Multifunctional role of GPCR signaling in epithelial tube formation

Vishakha Vishwakarma, Thao Phuong Le, and SeYeon Chung*

Department of Biological Sciences, Louisiana State University, Baton Rouge, LA 70803, USA

*Author for correspondence: seyeonchung@lsu.edu

Key words: *Drosophila*, Salivary gland, Fog signaling, GPCR, Actomyosin

Running title: GPCR signaling in tube formation

ABSTRACT

Epithelial tube formation requires Rho1-dependent actomyosin contractility to generate the cellular forces that drive cell shape changes and rearrangement. Rho1 signaling is activated by G protein-coupled receptor (GPCR) signaling at the cell surface. During *Drosophila* embryonic salivary gland (SG) invagination, the GPCR ligand Folded gastrulation (Fog) activates Rho1 signaling to drive apical constriction. The SG receptor that transduces the Fog signal into Rho1-dependent myosin activation has not been identified. Here, we reveal that the Smog GPCR transduces Fog signal to regulate Rho kinase accumulation and myosin activation in the apicomedial region of cells to control apical constriction during SG invagination. We also report on unexpected Fog-independent roles for Smog in maintaining epithelial integrity and organizing cortical actin. Our data supports a model wherein Smog regulates distinct myosin pools and actin cytoskeleton in a ligand-dependent manner during epithelial tube formation.

INTRODUCTION

The formation of three-dimensional tubes by invagination from flat epithelial sheets is a fundamental process in forming organs, such as lungs and kidneys (Andrew and Ewald, 2010). The *Drosophila* embryonic salivary gland (SG) is a premier model system to study the mechanisms underlying epithelial tube morphogenesis (Chung et al., 2014; Girdler and Röper, 2014). The SG begins as a two-dimensional plate of cells on the embryo surface. Neither cell division nor cell death occurs once the SG cells are specified; all the morphogenetic changes arise by changes in cell shape and rearrangement.

A major cell shape change during SG invagination is apical constriction, wherein the apical side of epithelial cells shrinks while keeping the nearly constant volume (Lubarsky and Krasnow, 2003; Martin and Goldstein, 2014). During stage 11, SG cells begin to invaginate at the dorsal/posterior region of the placode through apical constriction (Fig. 1A). This leads to forming a narrow invagination pit through which all SG cells eventually internalize. Apical constriction is observed in both invertebrates and vertebrates, driving morphogenetic processes ranging from gastrulation in *Drosophila* and *Xenopus* to lens formation in the mouse eye to formation of tubular organs such as the *Drosophila* SG and chicken lungs (Kim et al., 2013; Myat and Andrew, 2000; Plageman et al., 2011; Sweeton et al., 1991). Defects in apical constriction result in defects in overall tissue shape, suggesting that coordinated apical constriction is required for final tissue architecture (Chung et al., 2017; Guglielmi et al., 2015; Izquierdo et al., 2018).

Contractile actomyosin networks generate the cellular forces driving coordinated cell behaviors during epithelial morphogenesis (Gorfinkiel and Blanchard, 2011; Levayer and Lecuit, 2012; Munjal and Lecuit, 2014). Non-muscle myosin II (hereafter referred to as myosin) uses its motor activity to pull on actin filaments anchored to adherens junctions (AJs) to apply tension on the junction and neighboring cells. Three distinct pools of myosin generate the contractile forces required for SG invagination (Booth et al., 2014; Chung et al., 2017; Röper, 2012). Apicomedial myosin forms in the center of the apical side of the SG cell and drives apical constriction (Booth et al., 2014; Chung et

al., 2017; Röper, 2012). Junctional myosin, associated with AJs of SG cells, is involved in cell intercalation (Sanchez-Corrales et al., 2018). A supracellular myosin cable surrounding the entire SG placode generates the tissue-level compressing force (Chung et al., 2017; Röper, 2012). From studies in the past several years by us and others, we are beginning to understand how each myosin pool is created and regulated during SG invagination (Booth et al., 2014; Chung et al., 2017; Le and Chung, 2021; Röper, 2012; Sanchez-Corrales et al., 2018; Sidor et al., 2020).

Localized activation of the RhoA (Rho1 in *Drosophila*) GTPase is key to creating and/or polarizing contractile myosin structures in epithelial cells (Blanchard et al., 2010; Dawes-Hoang et al., 2005; Martin et al., 2009; Mason et al., 2013). Studies in *Drosophila* have identified the Folded gastrulation (Fog) pathway as a key signaling pathway regulating Rho1 signaling during epithelial morphogenesis (Manning and Rogers, 2014). During *Drosophila* gastrulation, two G protein-coupled receptors (GPCRs), Smog (ubiquitously expressed) and Mist (mesoderm-specific), respond to Fog to activate heterotrimeric G proteins, Rho1, and Rho kinase (Rok) to regulate myosin contractility (Costa et al., 1994; Dawes-Hoang et al., 2005; Kerridge et al., 2016; Kölsch et al., 2007; Manning et al., 2013; Mason et al., 2013; Parks and Wieschaus, 1991). In our previous study in the SG, we also revealed a tissue-specific regulation of Fog signaling to activate myosin contractility: the Fork head (Fkh) transcription factor regulates SG upregulation of *fog*, which promotes accumulation of Rok and myosin specifically in the apicomedial region of SG cells to drive clustered apical constriction (Chung et al., 2017; Fig. 1A). Yet, it is unknown how the Fog signal is sensed and transduced into downstream Rho1 signaling during epithelial tube formation.

Studies in early *Drosophila* embryos have suggested a role of GPCR signaling as a common module for Rho1 activation in different subcellular regions of the cell. In the mesoderm, Smog and Mist function together to activate myosin in the apicomedial region of cells to drive apical constriction (Kerridge et al., 2016). In the ectoderm, where no apical constriction occurs, Smog is required for junctional myosin activation to drive cell intercalation (Kerridge et al., 2016). Recent work further has shown that distinct RhoGEFs activate myosin contractility in the apical and junctional domain of epithelial

101 cells under the control of specific G proteins in early *Drosophila* embryos (Garcia De
102 Las Bayonas et al., 2019). However, whether all three myosin pools in the SG are
103 regulated by independent mechanisms or by a common module during epithelial tube
104 formation remains unclear.

105 The contractile force of the actomyosin networks causes an increase of hydrostatic
106 pressure in the cytoplasm (Charras et al., 2005). During epithelial morphogenesis, cells
107 maintain the surface integrity by proper organization of actin at the cell cortex. Loss of
108 organized cortical actin networks leads to the formation of blebs, spherical protrusions
109 of the plasma membrane (Charras, 2008). During *Drosophila* gastrulation, blebs
110 occasionally arise during apical constriction of mesodermal cells; these blebs correlate
111 with apical F-actin holes (Costa et al., 1994; Jodoin et al., 2015). Disruption of cortical
112 actin by latrunculin B, which sequesters globular actin (G-actin) and prevents
113 filamentous actin (F-actin) assembly, enhances blebbing in epithelial cells in early
114 *Drosophila* embryos (Kanesaki et al., 2013). Mutations in heterotrimeric G proteins also
115 enhance blebbing (Kanesaki et al., 2013), suggesting a role of G proteins in stabilizing
116 cortical actin. The mechanisms of cortical actin regulation during epithelial tube
117 formation are not well understood.

118 Here, we reveal multiple roles of Smog GPCR in regulating actomyosin networks during
119 *Drosophila* SG tube formation. We show that the GPCR Smog transduces Fog signal to
120 regulate myosin contractility in the apicomedial region of SG cells to drive apical
121 constriction during SG invagination. Our study supports a model wherein Smog
122 regulates apicomedial and junctional/supracellular myosin pools in a Fog-dependent
123 and -independent manner, respectively. We further reveal new roles of Smog in
124 regulating the microtubule networks, key apical and junction proteins, and cortical actin
125 organization during SG invagination, suggesting multifunctional roles of GPCR signaling
126 during epithelial tube formation.

127 **RESULTS**

128 **Smog transduces Fog signal in the SG**

129 To test the role of Smog in transducing Fog signal during SG invagination, we first
130 examined *smog* transcripts and Smog protein levels in the developing SG. Consistent
131 with the ubiquitous expression of *smog* (Kerridge et al., 2016), fluorescent in situ
132 hybridization revealed low levels of *smog* mRNA expression in the entire embryo,
133 including the SG. Strong *smog* mRNA signals were observed in SG cells near the
134 invagination pit (Fig. 1B, B'), potentially due to the shrinking apical domain in those
135 cells. We also examined Smog protein localization in the SG using a functional Smog-
136 GFP fusion protein expressed under the control of the *sqh* promoter (Kerridge et al.,
137 2016). Smog-GFP signals were detected as small punctate structures enriched near
138 AJs in SG cells (Fig. 1C-C''). Importantly, Smog-GFP signals were dramatically
139 increased in the entire apical domain of Fog-overexpressing SGs (Fig. 1D-D'';
140 quantification in Fig. 1E), suggesting that Smog is recruited to the apical domain of SG
141 cells by overproduced Fog.

142 To test whether Smog transduces Fog signal in the SG to regulate myosin contractility,
143 we performed a genetic suppression test. We hypothesized that if Smog is a SG
144 receptor for Fog, knocking down *smog* in the SG should suppress the gain-of-function
145 effect of Fog. We used sqh-GFP, a GFP-tagged version of myosin regulatory light chain
146 (Royou et al., 2004), and Rok-GFP, a GFP-tagged Rok fusion protein (Abreu-Blanco et
147 al., 2014), as readouts of Fog signaling. sqh-GFP signals were significantly increased in
148 the apicomedial region of Fog-overexpressing SG cells (compare Fig. 1G', G''' to Fig.
149 1F', F'''; quantification in Fig. 1H), suggesting increased myosin levels by Fog
150 overexpression. Notably, sqh-GFP signals at AJs of SG cells were not significantly
151 changed (Fig. 1I), suggesting that Fog promotes Rok accumulation and myosin
152 activation in the apicomedial region of SG cells. Fog-overexpressing SG cells showed
153 highly distorted AJs (Fig. 1G, G'') compared to control SG cells (Fig 1F, F''), suggesting
154 increased pulling forces due to increased apicomedial myosin in Fog-overexpressing
155 SG cells. Consistent with our finding that Fog signal promotes accumulation of Rok in
156 the apicomedial region of SG cells (Chung et al., 2017), quantification of areas occupied
157 by Rok-GFP puncta revealed overaccumulated Rok-GFP signals in the apicomedial

158 region of Fog-overexpressing SG cells (compare Fig. 1L', L''' to Fig. 1K', K''';
159 quantification in Fig. 1N). Knockdown of *smog* in the SG using RNA interference (RNAi)
160 and the SG-specific *fkh-Gal4* driver (Henderson and Andrew, 2000) both suppressed
161 the apicomedial accumulation of Rok-GFP signals and reduced the magnitude of AJ
162 distortion (Fig. 1M-M'''; quantification in 1N, O). These data suggest that Smog
163 transduces Fog signal in the SG to facilitate Rok and myosin accumulation in the
164 apicomedial region of SG cells.

165

166 **Smog-transfected *Drosophila* S2 cells contract upon Fog signal**
167 To further test the role of Smog in transducing Fog signal to regulate myosin
168 contractility, we performed an in vitro cell contraction assay using *Drosophila* S2 cells.
169 S2 cells do not express Fog receptors, and therefore, do not respond to Fog in the
170 normal culture condition (Manning et al., 2013; Fig. 2A-B'). As shown in a previous
171 study (Manning et al., 2013), S2 cells transfected with Mist, the mesoderm-specific
172 receptor for Fog, contracted robustly when cultured in Fog-containing media (Fig. 2C-
173 D'). Since Smog was not detectable in *Drosophila* S2 cells (modENCODE Cell Line
174 Expression Data; Flybase), we tested if S2 cells transfected with Smog also contract
175 upon Fog treatment. Indeed, Smog-transfected cells showed a significantly higher
176 percentage of contraction upon Fog treatment compared to non-transfected S2 cells
177 (Fig. 2A-B', E-F'; quantification in Fig. 2G). Thus, Smog can transduce Fog signal to
178 regulate cellular contractility both in the SG and in vitro.

179

180 **Smog is required for apical constriction in the SG and epithelial morphogenesis**
181 **during embryogenesis**
182 To test the possibility that Smog functions as a Fog receptor in the SG, we knocked
183 down *smog* in the SG (using *fkh-Gal4*) using RNAi and compared apical areas of SG
184 cells to those in *fog* mutants. Two independent short hairpin RNAi lines,
185 *TRiP.HMC03192* (a stronger line; Fig. 3B, B'; also used for genetic suppression assay
186 in Fig. 1J-J''') and *TRiP.GL01473* (a weaker line; Fig. S1C, C'), were used. Cell

187 segmentation analysis revealed that SG cells with smaller apical areas showed a less
188 coordinated spatial distribution in *smog* RNAi SGs compared to control (Fig. 3A-B'; Fig.
189 S1B-C'), similar to the previously reported *fog* mutant phenotype (Chung et al., 2017;
190 Fig. S1A, A'). Quantification of percentage and cumulative percentage of cells of
191 different apical areas also revealed that SGs with *smog* knockdown with either RNA line
192 show larger apical areas compared to control (Fig. 3G; Fig. S1D), suggesting defective
193 apical constriction upon *smog* knockdown.

194 Since *smog* has a strong maternal contribution (Flybase Developmental RNA-Seq), we
195 also knocked down *smog* both maternally (using *matα-Gal4*; Häcker and Perrimon,
196 1998) and zygotically in the SG (using *fkh-Gal4*) and observed slightly more severe
197 apical constriction defects in SG cells (hereafter referred to as *smog* M/Z knockdown;
198 Fig. 3C, C'; quantification in 3G). Maternal knockdown of *smog* using the stronger RNAi
199 line (*TRiP.HMC03192*) resulted in severe defects in egg-laying. Therefore, all M/Z
200 knockdown experiments were performed using the weaker line (*TRiP.GL01473*).
201 Consistent with the ubiquitous expression of *smog* and its role in epithelial
202 morphogenesis in the early *Drosophila* embryo (Kerridge et al., 2016), *smog* M/Z
203 knockdown also resulted in a slight disruption of the overall embryonic morphology,
204 including defects in the head region, a wavy embryo surface, and an irregular ventral
205 midline (Fig. 3M, N). Unlike the circular SG placode of WT, *smog* M/Z knockdown also
206 resulted in a SG placode that was elongated along the dorsal/ventral axis (compare Fig.
207 3A, A' to 3C, C'). 3D reconstruction of confocal images revealed disrupted epithelial
208 morphology in *smog* M/Z knockdown, with wide and wavy grooves, enlarged epithelial
209 cells, and an elongated SG placode (Fig. 3I, J).

210 *smog* zygotic null mutants (Kerridge et al., 2016) had a range of defects similar to those
211 observed with *smog* knockdown. 73.8% of embryos (59/80) showed relatively normal
212 embryonic morphology with mild apical constriction defects in SG cells, like *smog*
213 zygotic knockdown (classified as '*smog* null [mild]'; Fig. 3D-E', K; quantification in 3H);
214 26.2% of embryos (21/80) showed a disrupted embryonic morphology with SGs
215 elongated along the dorsal/ventral axis (Fig. 3F, F', L) and more severe apical
216 constriction defects (Fig. 3H), like *smog* M/Z knockdown (classified as '*smog* null

217 [severe]'). All embryos at late stages (stages 15-17) *smog* null mutants showed
218 relatively normal embryonic morphology (Fig. S2A, B), suggesting that severely
219 defective embryos with *smog* loss do not survive/develop past stage 14. Notably, these
220 embryos have relatively normal internalized SGs (Fig. S2F, G), except for rare cases of
221 crooked SG morphology (Fig. S2D), confirming our previous finding that apical
222 constriction is not required for SG internalization (Chung et al., 2017). Altogether, these
223 data suggest that Smog is required for coordinated apical constriction during SG
224 invagination and proper epithelial morphogenesis during embryogenesis.

225

226 **Smog regulates apicomedial and junctional myosin in a Fog-dependent and -**
227 **independent manner in the SG**

228 We next examined myosin levels and distribution in the SGs in *smog* knockdown or
229 *smog* mutants using sqh-GFP. Apicomedial myosin, which generates the pulling force
230 for apical constriction during SG invagination (Booth et al., 2014), is the only myosin
231 pool defective in the SGs of *fog* mutants (Chung et al., 2017). Consistent with the idea
232 that Smog transduces Fog signal in the SG, both *smog* knockdown (either zygotic or
233 M/Z knockdown) and *smog* loss resulted in a significant reduction in the intensity of
234 apicomedial myosin in SG cells near the invagination pit, compared to control (Fig. 4 A-
235 D''; quantification in 4I). Moreover, compared to clear web-like structures of apicomedial
236 myosin in control SG cells (Fig. 4A-A''), SG cells in *smog* knockdown or *smog* null
237 mutants showed reduced areas of sqh-GFP puncta, suggesting dispersed myosin along
238 the entire apical surface in SG cells (Fig. 4K). Interestingly, the intensity of junctional
239 myosin was also significantly reduced in SG cells with *smog* knockdown or *smog* loss,
240 compared to control (Fig. 4A-D'', quantification in 4J). This phenotype is distinct from
241 what was observed in *fog* mutants, where junctional myosin was unaffected in SG cells
242 (Chung et al., 2017). We conclude that Smog is required for maintaining normal levels
243 of both apicomedial and junctional myosin in the SG in a Fog-dependent and -
244 independent manner, respectively.

245 We also tested Rok distribution in SG cells in *smog* RNAi and *smog* null mutants, using
246 Rok-GFP. Consistent with our previous study (Chung et al., 2017), Rok-GFP formed
247 large punctate structures in the apicomedial region in control SG cells (Fig. 4E-E'').
248 However, Rok-GFP failed to accumulate and was dispersed along the entire apical
249 domain in SG cells in *smog* knockdown and *smog* null mutants (Fig. 4F-H'';
250 quantification in 4L), similar to the dispersed Rok-GFP distribution observed in *fog*
251 mutant SG cells (Chung et al., 2017). These data suggest that Smog is required for Rok
252 accumulation in the apical domain of SG cells.

253

254 ***smog* loss leads to defects in the tissue-level myosin cable**

255 Reduced myosin levels and the elongated SG placode in *smog* null [severe] embryos
256 led us to test the third pool of myosin in the SG, the supracellular myosin cable
257 surrounding the SG placode. Consistent with the idea that this myosin cable is under
258 tension (Chung et al., 2017; Röper, 2012), WT SGs showed a relatively smooth tissue
259 boundary (Fig. 4M-M''). However, SGs in *smog* null [severe] embryos showed an
260 irregular boundary and a less clear myosin cable (Fig. 4N-N''). We calculated the
261 circularity of the SG placode as a measure of smoothness and tension of the SG
262 boundary. The circularity of the WT placode was significantly higher than the circularity
263 of one cell row inside (inner boundary) or outside of SG placode (outer boundary),
264 suggesting a higher tension of the myosin cable in WT (Fig. 4O, P). Consistent with the
265 irregular SG boundary in *smog* null [severe], the circularity of the SG placode in *smog*
266 null embryos was significantly lower than that of WT and was not statistically significant
267 from the inner or outer boundaries, suggesting a lack of tension at SG boundary in
268 *smog* null mutants (Fig. 4P). Overall, our data suggest that the loss of *smog* affects all
269 myosin pools in the SG, including the myosin at the SG boundary, leading to reduced
270 tension at the SG boundary and defects in generating the compressing force.

271

272 **Smog is required for proper localization of apical and junctional components and**
273 **microtubule networks in epithelial cells**

274 Since we observed a range of defects in whole embryo morphology in *smog* mutants,
275 we explored the potential cellular basis. In stage 11 *smog* null [severe] embryos, we
276 occasionally observed large areas in the epidermis and the SG where E-Cad (Fig. 5B,
277 B') and Crb (Fig. 5D, D') signals were absent or significantly reduced. Similar defects
278 were observed in late-stage (stage 14) embryos. Crb levels were significantly reduced
279 in large areas; in the most severe cases, Crb was dispersed in the entire epidermis (Fig.
280 S3B, B'). These data suggest that Smog is required for maintaining epithelial polarity
281 and junctional integrity by regulating E-Cad and Crb levels or distribution.
282 To better understand the basis of the reduced E-Cad and Crb in *smog* mutants, we
283 examined *smog* null mutant SG cells at higher magnification. Even SGs that do not
284 contain large patches where E-Cad/Crb are missing showed discontinuous E-Cad/Crb
285 signals, resulting in small gaps in signal along the SG cell boundary (Fig. 5F, G, I, J).
286 Such gaps were observed in both *smog* null [mild] and *smog* null [severe] embryos.
287 Although the number and the length of gaps in E-Cad signals in *smog* null [mild] were
288 comparable to those of WT, they were significantly higher in *smog* null [severe]
289 compared to WT (Fig. 5F, G; quantification in 5K, L). The number and the length of
290 gaps in Crb signals in SG cells were significantly higher in both mild and severe *smog*
291 null mutant embryos compared to WT (Fig. 5I, J; quantification in 5M, N). These data
292 suggest a role of Smog in regulating Crb and E-Cad levels and continuity during
293 epithelial morphogenesis, including the SG.

294 Anisotropic localization of Crb at the SG boundary has been suggested to drive the
295 formation of supracellular myosin cable in SG (Röper, 2012). Consistent with this, in
296 control SGs, Crb levels were higher in the junctions that did not contribute to the myosin
297 cable, whereas myosin was highly enriched at the junction forming the cable at the SG
298 boundary (Fig. S3C-E'''). However, in several *smog* null [severe] SGs, the overall Crb
299 intensity was quite low, and Crb did not show an anisotropic localization at the SG
300 boundary (Fig. S3F-H''). This data suggests that *smog* loss results in the reduction of
301 both myosin and Crb, failing to form the supracellular myosin cable at the SG boundary.

302 Microtubules are required for forming and maintaining apical myosin structures (Booth
303 et al., 2014; Ko et al., 2019) and for transporting several key apical and junctional

304 proteins in *Drosophila* tubular organs, including E-Cad and Crb (Le and Chung, 2021; le
305 Droguen et al., 2015). We recently showed that microtubule-dependent intracellular
306 trafficking has an important role in regulating apical constriction and apicomedial myosin
307 during SG invagination (Le and Chung, 2021). To examine the microtubule networks in
308 the SG of wild-type and *smog* mutant embryos, we stained with antibodies against
309 acetylated-α-tubulin, a marker of stable, long-lived microtubules, and tyrosinated-α-
310 tubulin, a marker of dynamic, short-lived microtubules (Westermann and Weber, 2003).
311 We observed a reduction of both acetylated-α-tubulin and tyrosinated-α-tubulin signals
312 in the apical region of the SG in *smog* mutants, compared to wild type (compare Fig.
313 5O, Q to Fig. 5P, R; quantification in 5S), suggesting disrupted microtubule networks in
314 the SG in *smog* mutants. This finding suggests that loss of *smog* could affect apical
315 pools of myosin, Crb and E-Cad through effects on microtubule abundance, distribution
316 and/or polarity.

317

318 **Smog is required for cortical actin organization in the SG**

319 We observed numerous blebs in the apical membrane of SG cells in *smog* null [severe]
320 mutants, which were most prominent near the invagination pit (compare Fig. 6A-A''' to
321 Fig. 6B-B'''). Such blebs were not observed in SGs in WT, *smog* null [mild], or *fog*
322 mutant embryos (Fig. S4A-C''). Unlike dispersed Rok-GFP signals in *smog* knockdown
323 or *smog* null [mild] embryos (Fig. 4F-H''), Rok-GFP was enriched in many of these blebs
324 (Fig. 6B-B'''), consistent with Rok's recruitment to retracting blebs (Aoki et al., 2016). In
325 *smog* null [severe] embryos, blebs were also occasionally observed in cells outside the
326 SG placode (Fig. S4D-E''). During *Drosophila* gastrulation, bleb formation correlates
327 with cortical F-actin holes (Jodoin et al., 2015), and disruption of cortical actin enhances
328 blebbing (Kanesaki et al., 2013). We therefore tested if Smog affects the cortical actin
329 network during apical constriction in the SG. Indeed, phalloidin staining revealed that
330 whereas strong F-actin signals were observed in the apical domain of SG cells near the
331 invagination pit in WT, F-actin was significantly reduced in SGs in *smog* mutants (Fig.
332 6C-C', 6D-D').

333 Apical F-actin formation in *Drosophila* tubular organs requires the formin family actin
334 nucleator Diaphanous (Dia) (Massarwa et al., 2009; Rousso et al., 2013). Since the
335 apical localization and activity of Dia are critical for restricting F-actin formation to the
336 correct membrane domain, we tested the localization and levels of Dia in the SG in
337 *smog* mutants. Similar to reduced F-actin, we observed reduced Dia signals in the
338 apical domain of SG cells, most prominently near the invagination pit in *smog* mutants,
339 compared to WT (Fig. 6C-C'', D-D''). Quantification of the Dia intensity revealed that Dia
340 signals are reduced in the apicomedial but not in the junctional region of SG cells (Fig.
341 6E-G). Our data suggest that Smog is required for the cortical actin networks during SG
342 invagination, at least in part via modulating Dia levels.

343 We next tested if the reduction in actin levels in *smog* mutants is due to defects in actin
344 turnover. To test this, we modulated the level of actin regulators in the SG in *smog*
345 mutants and assayed the blebbing phenotype. Using RNAi, we knocked down
346 *chickadee* (*chic*), which encodes *Drosophila* profilin, a protein that increases F-actin by
347 promoting actin polymerization (Cooley et al., 1992), in the *smog* mutant background. If
348 there is a shift from F-actin to monomeric G-actin in *smog* mutants, we expect
349 enhancement of the disorganized actin phenotype and bleb formation with a reduced
350 *chic* level. Blebs were not observed in *smog* null [mild] embryos or in SGs knocked
351 down for *chic* in the otherwise wild-type background (Fig. 6H-H''; Fig. S4B-B'').
352 However, when *chic* was knocked down in the SG in the *smog* mutant background, we
353 observed enhanced blebbing even in mildly defective SG cells (Fig. 6I-I''). Since profilin
354 promotes formin-mediated actin filament assembly (Romero et al., 2004; Zweifel and
355 Courtemanche, 2020), our data suggests that reduced profilin by *chic* knockdown
356 aggravated defects in cortical actin organization with reduced Dia in *smog* mutants.
357 Overall, our data suggest that Smog is required for cortical actin organization as well as
358 myosin activation during epithelial morphogenesis.

DISCUSSION

Smog regulates different pools of myosin in a Fog-dependent and -independent manner during SG invagination

Fog signaling triggers epithelial cell shape changes driving tissue folding and invagination during development of *Drosophila* and other insects (Benton et al., 2019; Manning and Rogers, 2014). During *Drosophila* embryogenesis, *fog* is upregulated in multiple tissues undergoing apical constriction and tissue invagination, such as ventral furrow (mesoderm), the posterior midgut (endoderm), and the SG (ectodermal derivative) (Nikolaidou and Barrett, 2004). During *Drosophila* gastrulation, the ubiquitously expressed GPCR Smog and the mesoderm-specific GPCR Mist respond to Fog signal to regulate myosin contractility during mesoderm invagination (Kerridge et al., 2016; Manning et al., 2013). Here, we provide evidence that Smog functions as a SG receptor for Fog to activate myosin during SG invagination. Knockdown of *smog* by RNAi suppresses the gain-of-function effect of Fog in the SG (Fig. 1). Also, Smog-transfected S2 cells contract upon Fog signal (Fig. 2), suggesting that Smog responds to Fog to regulate myosin contractility both in vivo and in vitro. Our data show that Fog overexpression leads to Smog recruitment to the apicomedial region of SG cells (Fig. 1). Consistent with our data, Fog overexpression induces oligomerization of Smog in early *Drosophila* embryos (Jha et al., 2018).

Our study also dissects the roles of Smog in myosin activation during SG morphogenesis and reveals Fog-independent roles of Smog. Whereas *fog* mutants exhibit a decrease in only the apicomedial myosin pool in SG cells (Chung et al., 2017), *smog* loss and SG-specific knockdown of *smog* result in a significant reduction of both apicomedial and junctional myosin (Fig. 4). We propose that Smog regulates junctional myosin during epithelial morphogenesis in response to an unknown, ubiquitously expressed ligand and regulates apicomedial myosin in response to Fog in tissues with high Fog signals, such as the mesoderm (Kerridge et al., 2016; Manning et al., 2013) and the SG (this study). Consistent with this model, during *Drosophila* gastrulation, Smog activates different myosin pools in tissues with different Fog levels. In the mesoderm, where Fog levels are high, Smog and Mist transduce Fog signal to activate myosin in the apicomedial region and drive apical constriction. In the ectoderm, where

390 Fog levels are very low, Smog is required for junctional myosin activation to drive cell
391 intercalation. SG cells undergo both apical constriction and cell intercalation, and our
392 data shows that Smog regulates both pools of myosin in the SG in a Fog-dependent
393 and -independent manner. It is possible that in tissues with high Fog signals, an
394 additional tissue-specific GPCR(s) function with Smog in response to Fog to fine-tune
395 the Fog signaling for proper apical constriction, like Mist does in the mesoderm. It will be
396 interesting to determine whether additional SG-specific GPCRs function with Smog
397 during SG invagination.

398 The downstream components that transduce signals from the Smog GPCR to regulate
399 myosin in distinct regions of SG cells await discovery. Good candidates include two Rho
400 guanine nucleotide exchange factors (RhoGEFs), RhoGEF2 and Dp114RhoGEF, which
401 have been shown to activate Rho1 signaling at the apicomedial and junctional domain
402 of epithelial cells, respectively (Garcia De Las Bayonas et al., 2019). This process
403 requires upstream activation by heterotrimeric G proteins $G\alpha_{12/13}$/Cta and Gβ13F/Gγ1 at
404 the apicomedial and junctional domains, respectively (Garcia De Las Bayonas et al.,
405 2019). Thus, distinct ligand-receptor binding with Smog may activate distinct G proteins
406 and/or RhoGEFs in the apicomedial and junctional domains.

407

408 **Smog regulates cortical actin organization during SG invagination independent of**
409 **Fog**

410 We also discover that Smog regulates cortical F-actin organization during SG
411 invagination (Fig. 6). *smog* loss significantly reduces levels of F-actin and the formin
412 protein Dia (Fig. 6). Rho1 regulates actin polymerization via Dia (Goode and Eck, 2007),
413 and apical F-actin formation in the *Drosophila* SG requires apical localization and
414 activity of Dia (Massarwa et al., 2009; Rousso et al., 2013). Our data suggest that Smog
415 activates Rho1 signaling to regulate both cortical F-actin (via Dia) and myosin (via Rok)
416 (Fig. 7). Since mutations in *fog* do not enhance blebbing during SG invagination (Fig.
417 S4), Smog's role in regulating cortical actin is independent of Fog. Supporting our data,
418 during *Drosophila* gastrulation, *fog* mutants show normal GFP-Moesin signals in the

419 ventral furrow, suggesting normal cortical actin organization upon *fog* loss (Kanesaki et
420 al., 2013). $G\alpha_{12/13}$/Cta is a key component downstream of Fog that recruits RhoGEF2 to
421 the apical membrane to regulate myosin contractility (Barrett et al., 1997; Dawes-Hoang
422 et al., 2005). Interestingly, mutations in Gαi (G-iα65A) and Gβ13F/Gγ1, but not
423 $G\alpha_{12/13}$/Cta, disrupt cortical actin organization in early *Drosophila* embryos (Fox and
424 Peifer, 2007; Kanesaki et al., 2013). Therefore, Smog may signal through Gαi and/or
425 Gβ13F/Gγ1 to organize cortical actin, independent of Fog and $G\alpha_{12/13}$/Cta.

426 The link between heteromeric G proteins and Rho1 signaling occurs through activation
427 of specific RhoGEFs (Vázquez-Victorio et al., 2016). Actin polymerization resulting from
428 Fog-independent Smog activation may imply the recruitment of distinct proteins
429 modulating the activation of Rho1-mediated pathways. For example, in the absence of
430 Fog, a specific RhoGEF(s) downstream of Gαi or Gβ13F/Gγ1 may link Smog and Rho1
431 signaling to regulate cortical actin organization; upon high Fog signals, a different Rho1
432 modulator(s) downstream of $G\alpha_{12/13}$/Cta may be recruited to facilitate apicomedial
433 myosin formation. Further work is needed to identify the link between Smog and Rho1
434 activation in the presence or absence of Fog during SG invagination. It will be also
435 interesting to determine whether Fog-independent roles of Smog–regulating cortical
436 actin and junctional myosin–involve common or distinct Rho1 modulators.

437

438 **Smog regulates epithelial integrity during development**

439 *smog* null mutant embryos show a range of defects, allowing us to dissect the roles of
440 Smog in epithelial morphogenesis. Our data reveal that Smog is required for epithelial
441 integrity by affecting levels and localization of Crb and E-Cad (Fig. 5). Since the
442 decrease in the level of Crb and E-Cad in *smog* mutants correlates with significantly
443 reduced myosin levels, disrupted epithelial integrity may be due to disrupted actomyosin
444 networks. Myosin II is critical for cells to concentrate E-cadherin at cell-cell contacts
445 (Shewan et al., 2005). In early *Drosophila* embryos, the absence of contractile myosin
446 leads to the disassembly of junctions (Weng and Wieschaus, 2016). A possible scenario
447 is that Smog is required to recruit key Rho1 regulators, such as RhoGEF2,

448 Dp114RhoGEF, or other SG-upregulated RhoGEFs, to AJs during SG invagination to
449 promote junctional myosin assembly. Since Dia helps coordinate adhesion and
450 contractility of actomyosin (Homem and Peifer, 2008) and formin-mediated actin
451 polymerization at AJs stabilizes E-Cad and maintains epithelial integrity (Rao and
452 Zaidel-Bar, 2016), reduced Dia levels in *smog* mutants may also contribute to loss of
453 epithelial integrity.

454 Reduced and discontinuous signals of apical and junctional components in *smog*
455 mutant embryos can also be due, in part, to compromised intracellular trafficking.
456 Disorganized microtubule networks in SGs in *smog* mutants (Fig. 5) support this idea.
457 Our recent study showed that microtubule- and Rab11-dependent intracellular
458 trafficking regulates apical myosin pools and apical constriction during SG invagination,
459 via apical enrichment of Fog and the continuous distribution of Crb and E-Cad along
460 junctions (Le and Chung, 2021). The mechanism of how Smog affects microtubule
461 organization remains to be revealed. Overall, our findings suggest the multifaceted roles
462 of Smog during epithelial tube formation in regulating distinct myosin pools and cortical
463 actin in different subcellular domains in a ligand-dependent manner.

464 **MATERIALS AND METHODS**

465 **Fly stocks and genetics**

466 The fly stocks used in this study are listed in Table S1. All the crosses were performed
467 at 25°C.

468

469 **Immunofluorescence and confocal microscopy**

470 *Drosophila* embryos were collected on grape juice agar plates supplemented with yeast
471 paste at 25℃. Embryos were dechorionated with 50% bleach. For most samples,
472 embryos were fixed in 1:1 heptane: formaldehyde for 40 minutes and devitellinized with
473 80% EtOH. For Rok-GFP, Sqh-GFP, and phalloidin staining, embryos were hand-
474 devitellinized. Embryos were then stained with primary and secondary antibodies in
475 PBSTB (1X PBS with 0.1% Triton X-100 and 0.2% bovine serum albumin) and PBTr
476 (1X PBS with 0.1% Triton X-100) for EtOH devitalization and hand-devitalization,
477 respectively. Antibodies used in our experiments are listed in Table S2. Embryos were
478 mounted in Aqua-Poly/Mount (Polysciences, Inc) and imaged with a Leica TCS SP8
479 confocal microscope using 63x, NA 1.4 and 40x, NA 1.3 objectives. Images were
480 acquired as z-stacks (each 0.3 μm apart) that span the apical and junctional domains of
481 cells in the SG placode.

482

483 **Fluorescent in situ hybridization**

484 Embryos were fixed using formaldehyde/heptane for 30 min followed by devitellinization
485 with methanol. SP6 polymerase-synthesized digoxigenin (DIG)-labeled antisense probe
486 was prepared using the following primers: *smog*-F, 5'-ACAGAGCCCACCTGTGTAGG-
487 3'; *smog*-R, 5'-TCGCTGATCGAAAATGATCTC-3'. Fluorescent in situ hybridization was
488 performed using standard methods as described in (Knirr et al., 1999). Briefly, the
489 embryos were pre-hybridized for 1 hour at 56°C post-fixation. Following this step, the
490 embryos were hybridized with the probe overnight at 56°C. The next day, embryos were
491 stained for DIG using the anti-DIG primary antibody and biotin-conjugated secondary
492 antibody. The embryos were then incubated with AB solution (PK-6100, VECTASTAIN
493 Elite ABC kit). Tyramide signal amplification reaction was performed using Cy3
494 fluorescent dye (diluted 1:50 using amplification diluent) (Perkin Elmer Life Sciences,

495 Inc., NEL753001kt). The embryos were co-stained with CrebA and Crb antibodies for
496 visualizing SG nuclei and apical cell boundaries, respectively.
497
498 **Total Smog-GFP intensity**
499 Maximum intensity projections of two z-sections that span the apical and the junctional
500 region of SG cells were used. Intensity means of Smog-GFP signals of SG cells in the
501 entire SG placode were measured using Imaris software. The mean intensity of Smog-
502 GFP was normalized by the median deviation. The integrated density of Smog-GFP
503 was calculated by multiplying the apical area of the cell with the mean intensity of each
504 cell. Total Smog-GFP signals within the whole placode were calculated as the sum of
505 the integrated density of all cells. For background correction, mean gray values of
506 Smog-GFP in ten cells outside of the SG placode were measured. The average value of
507 mean gray values of Smog-GFP in these ten cells was used to subtract the background
508 of the cells inside the placode from the same embryo. Four and five SGs were used to
509 quantify control and Fog overexpression, respectively. P values were calculated using
510 Welch's t-test in the GraphPad Prism software.
511
512 **Cell segmentation and apical area quantification**
513 SGs that were invaginated within the range of 4.8-9.9 μm depth were used for
514 quantification. Two or three z-sections of the apical domain were used to generate a
515 maximum intensity projection (Leica LasX software). SG cells were marked using CrebA
516 and segmented along E-Cad signals using the Imaris program. Apical areas of
517 segmented cells were calculated using Imaris, and cells were color-coded based on
518 their apical domain size. Frequency distribution was performed using GraphPad Prism.
519 Apical areas from eight SGs were quantified in control, *smog* knockdown (Z), and *smog*
520 null [mild] embryos. Six SGs were used for quantification for *smog* knockdown (M/Z)
521 and *smog* null [severe] embryos. Statistical significance was determined using Mann-
522 Whitney U test (percentage of cells) and Kolmogorov-Smirnov test (cumulative
523 percentage of cells).
524

525 **Quantification of myosin and Dia intensity in the apicomedial and junctional**
526 **domains**
527 Maximum intensity projection of two z-sections spanning apical and junctional regions of
528 SG cells with Sqh-GFP and E-Cad signals was used. The images were then exported to
529 ImageJ and converted to RGB stack image type. Twenty cells near the invagination pit
530 in each of five SGs were used for quantification. To calculate the apicomedial and
531 junctional myosin intensity, regions were drawn manually along the inner and outer
532 boundary of the E-Cad signal of each cell, and mean gray values were measured for
533 apicomedial and junctional myosin. For background subtraction, the average mean gray
534 value of sqh-GFP signals for ten cells outside the SG placode was subtracted from the
535 mean gray value of apicomedial and junctional myosin for each SG cell. SuperPlots
536 (Lord et al., 2020) were used to address the variability of datasets in each SG. Each
537 data point in the graph represents one SG consisting of twenty cells used for
538 quantification. Statistical significance was determined using Welch's t-test. Dia intensity
539 in the apicomedial and junctional domain of SG cells was quantified using the same
540 strategy, with ten cells near the invagination pit in each of five SGs.
541
542 **Quantification of areas of Rok-GFP and apicomedial myosin particles**
543 A single z-section of the confocal image with the strongest Rok-GFP signals in the
544 apicomedial region was used. Rok-GFP signals were converted to black and white
545 using the threshold tool in Adobe Photoshop. Junctional Rok-GFP signals were
546 removed manually based on E-Cad signals. Areas of Rok-GFP puncta were determined
547 using the Analyze Particles tool in ImageJ. Rok-GFP puncta with area ≥0.02 μm^2 was
548 measured. Fifteen cells in the dorsal posterior region near the invagination pit of the SG
549 placode were used for quantification. The same strategy was used for Sqh-GFP signals
550 to quantify the area of apicomedial myosin. SuperPlots show mean values of data
551 points of five SGs. Statistical significance was determined using Welch's t-test.
552
553 **Quantification of the waviness of junctions**
554 Using a single z-section with the highest E-Cad signals and ImageJ software, the
555 shortest (L_0) and the actual distance (L) between vertices were measured in SG cells.

556 The ratio of these distances (L/L_0) was used as the waviness of junctions. 10-15 cells
557 near the invagination pit in each of five SGs were used for quantification. Statistical
558 significance was determined using Welch's t-test.
559
560 **Quantification of number and length of gaps of Crb and E-Cad**
561 The number and the length of gaps for Crb and E-Cad signals were measured using
562 confocal images and ImageJ. A single z-section with the highest Crb or E-Cad signals
563 was chosen for quantification. Gaps with a length ≥0.2 μm were used for quantification.
564 All junctions from ten cells in five SGs were quantified. If there were multiple gaps on a
565 junction, we added the length of all the gaps on that junction to calculate the ratio of the
566 length of gaps to junctional length. Statistical significance was determined using
567 Welch's t-test.
568
569 **Circularity of the SG boundary**
570 Using confocal images and ImageJ, cell boundaries were manually drawn along E-Cad
571 signals at the SG placode boundary and one cell row outside and inside the placode.
572 For most samples, strong myosin cable signals at the dorsal, anterior, and posterior
573 boundaries of the placode and CrebA signals in SG cells were used to determine the
574 SG boundary. In *smog* null [severe], where myosin signals were significantly reduced in
575 all cells, CrebA signals were used to determine the boundary. The ventral midline was
576 used as the ventral boundary of the SG in all cases. The perimeter and the area of the
577 SG corresponding to these boundaries were measured using ImageJ, and circularity
578 was calculated using the formula, $C = 4\pi \text{ area}/\text{perimeter}^2$. For a perfect circle, the value
579 of circularity should be 1. Five SGs were used for quantification, and statistical
580 significance was determined using Welch's t-test.
581
582 **Tyrosinated tubulin intensity quantification**
583 Three z sections spanning the most apical region of SG cells were used for
584 quantification. The mean intensity of tyrosinated tubulin signals in the whole SG placode
585 was measured using ImageJ. The area of the SG was drawn manually based on the E-
586 Cad and CrebA signals to label the cell boundary and SG nuclei, respectively. For

587 background correction, the mean intensity of ten cells outside the SG of the same
588 embryo was used. The ratio of the mean intensity of tyrosinated tubulin signals inside
589 the placode to the mean intensity of control cells outside the placode was calculated
590 and plotted. Four and five SGs were used for control and *smog* mutant, respectively. t-
591 test with Welch's correction was used to calculate the p value.
592

593 **Cell contractility assay**

594 cDNA clones for *smog* (RE70685) and *mist* (RE13854) were obtained from *Drosophila*
595 Genomics Resource Center (DGRC). Isolated cDNAs were cloned into the pMT-V5-
596 HisB vector (Addgene) using the conventional restriction digestion and ligation method.
597 Primers with restriction sites used to isolate the open reading frame are stated below
598 (restriction sites underlined).

599 *smog* CDS-EcoRI-5', 5'-CCGGAATTCATGGAACTGTGCATAGCAAC-3'
600 *smog* CDS-NotI-3', 5'-ATTTGCGGCCGCATTGGTCGTGATTGTATCTTTGG-3'
601 *mist* CDS-EcoRI-5', 5'-CCGGAATTCATGGACAGGAGTCGGAGTAGC-3'
602 *mist* CDS-NotI-3', 5'-ATTTGCGGCCGCAGCAAATGGTCTCCATTTTG-3'

603 S2 and S2-Mt-Fog-myc cells (Manning et al., 2013) were obtained from DGRC. Shields
604 and Sang M3 insect media (HiMedia) was used with 10% Fetal Bovine Serum (Corning)
605 and 1:1000 Antibiotic-Antimycotic (Gibco). Cells were cultivated at 25°C either in 25-cm^2
606 flask in 5 ml media or 75-cm^2 flask in 15 ml media. To prepare for the Fog media, S2-
607 Mt-Fog-myc cells were grown undisturbed for 4-8 days to attain approximately 100%
608 confluency. 50 µl of 100 mM CuSO4 was added to nearly 100% confluent cells in 75-
609 cm^2 flask to induce metallothionein promoter. The Fog-containing media was collected
610 by centrifugation and further concentrated using 3,000 MW concentrators. The
611 presence of Fog was confirmed by Western blot using the Myc-antibody (Invitrogen;
612 RRID:AB_2533008). Non-transfected S2 cells were used as a control.
613 Cell contractility assay was performed as described in (Manning et al., 2013). Smog- or
614 Mist-transfected S2 cells were induced with $CuSO_4$. Cells were then transferred to
615 Concanavalin A-coated coverslips and fixed using 10% paraformaldehyde in PBTr for
616 15 minutes at room temperature (RT). After being blocked in 5% NGS in PBTr for 20

617 minutes at RT, cells were stained with the V5 antibody (Invitrogen; RRID:AB_2556564)
618 to differentiate between transfected and non-transfected cells. Cell contractility of
619 transfected cells was monitored using a phase-contrast filter in a Leica DM2500
620 microscope using the 40X, 0.8 NA objective. Three independent experiments were
621 performed. Two-way ANOVA was performed to calculate statistical significance.
622
623 **Fly strains used (Table S1)**

Fly strain	**Sources and References**	**RRID**
Oregon R (wild type)		
fkh-Gal4	Henderson and Andrew, 2000	BDSC_78060
matα4-Gal4 (on II)	Bloomington Stock Center	BDSC_7062
matα4-Gal4 (on III)	Bloomington Stock Center	BDSC_7063
UAS-Fog	Dawes-Hoang et al., 2005	
smog-GFP	Kerridge et al., 2016	
ubi-Rok-GFP	Abreu-Blanco et al., 2014	BDSC_52289
sqh-GFP	Royou et al., 2004	BDSC_57144
sqh-mCherry	Martin et al., 2009	BDSC_59024
smog null mutant	Kerridge et al., 2016	
fog^{RA67}		BDSC_6218
UAS-Dicer-2	Vienna *Drosophila* Resource (#60008)	
TRiP.GL01473 (*smog* RNAi (weak))	Bloomington Stock Center	BDSC_43135
TRiP.HMC03192 (*smog* RNAi (strong))	Bloomington Stock Center	BDSC_51705
TRiP.HMS00550 (*chic* RNAi)	Bloomington Stock Center	BDSC_34523

624 **Antibodies Used (Table S2)**

Antibody	Source	RRID	Dilution
α-E-Cad (rat)	DSHB (DCAD2)	AB_528120	1:50
α-CrebA (rat)	Andrew lab (John Hopkins University); This study		1:3000
α-CrebA (rabbit)	Andrew lab (John Hopkins University)	AB_10805295	1:5000
α-GFP (chicken)	Invitrogen (A10262)	AB_2534023	1:500
α-β-galactosidase (rabbit)	Invitrogen (A11132)	AB_221539	1:500
α-β-galactosidase (mouse)	Invitrogen (MA5-15222)	AB_10980770	1:500
α-Crb (mouse)	DSHB (Cq4)	AB_528181	1:10
α-mCherry (rat)	Invitrogen (M11217)	AB_2536611	1:1000
α-Myc (mouse)	Invitrogen (13-2500)	AB_2533008	1:250
α-V5 (mouse)	Invitrogen (R960-25)	AB_2556564	1:400
α-Dia (rabbit)	Afshar et al., 2000		1: 5000
Phalloidin Alexa 488	Invitrogen (A12379)		1:250
Alexa Fluor 488/568/647-coupled secondary antibodies	Invitrogen		1:500

625

Acknowledgments

We thank the members of the Chung laboratory for comments and suggestions. We thank A. Martin, T. Lecuit and the Bloomington stock center for fly stocks, and D. J. Andrew and the Developmental Studies Hybridoma Bank for antibodies. We thank Flybase for the gene information. We are grateful to D. J. Andrew, C. D. Hanlon, J. Kim, and J. Matthew for their helpful comments on the manuscript. This work is supported by start-up fund from Louisiana State University and the grant from the Board of Regents Research Competitiveness Subprogram GR-00005224 to S.C.

634 **Figure Legends**

635 **Figure 1. Smog transduces Fog signal to activate Rok and myosin in the SG.** (A)
636 Cartoon diagram showing SG placodes (magenta) in the ventral side of a stage 11
637 *Drosophila* embryo. Cells that undergo apical constriction anterior to the invagination pit
638 (asterisk) are shown in purple. In those cells, the Fog ligand (yellow) binds to its GPCR
639 (blue) to activate apicomedial myosin. In all stage 11 SG images, anterior is to the left,
640 and dorsal is up. (B, B') Fluorescent in situ hybridization of *smog* (magenta) in the
641 invaginating WT SG. Strong *smog* mRNA signals are shown in apically constricting SG
642 cells near the invagination pit (arrowheads). CrebA (green), SG nuclei. White lines, SG
643 boundary. Arrows, *smog* signals near the grooves and the ventral midline. (C-D'')
644 Smog-GFP (green) signals in control (C-C'') and Fog-overexpressing SGs (D-D'').
645 Magenta, E-Cad. Control SG cells show puncta of Smog-GFP signals in the apical
646 region near AJs (yellow arrowheads). Considerably higher Smog-GFP signals in the
647 entire apical domain of Fog-overexpressing SG cells (red arrowheads). Insets,
648 magnified images of yellow boxed regions. (C'', D'') Z sections across the yellow lines in
649 C and D. (E) Quantification of total Smog-GFP intensity in control and Fog
650 overexpressing SG cells. n= 4 SGs (control); 5 SG (Fog overexpression). *p≤0.05
651 (Welch's t-test). (F, G) sqh-GFP (green) and E-Cad (magenta) signals in control (F) and
652 Fog-overexpressing (G) SGs. (F'-G''') Magnified images of yellow boxed regions in F
653 and G. Compared to control (F-F'''), sqh-GFP signals are increased in the apicomedial
654 region of Fog-overexpressing SG cells (G-G'''). Yellow arrowheads, AJs. Cyan
655 arrowheads, sqh-GFP signals. (H-J) Quantification of apicomedial myosin intensity (H),
656 junctional myosin intensity (I), and the ratio of apicomedial to junctional myosin intensity
657 (J). (K-M''') Rok-GFP (green) and E-Cad (magenta) signals in SGs. K'-M''', magnified
658 images of yellow boxed regions in K-M. Compared to control (K-K'''), Fog-
659 overexpressing SG shows overaccumulation of Rok-GFP and wavy cell junctions (L-
660 L'''). *smog* knockdown suppresses these phenotypes (M-M'''). Yellow arrowheads, AJs.
661 Cyan arrowheads, Rok-GFP puncta. (N, O) Quantification of the area of Rok-GFP
662 particles (N) and waviness of AJs (O). Asterisks, invagination pit. n=5 SGs, 75 cells for
663 each genotype in H-J, N, and O. *p≤0.05; **p≤0.01; ***p≤0.001; ****p≤0.0001 (Welch's t-
664 test).

665 **Figure 2. Smog-transfected S2 cells contract in response to Fog.** (A-F') S2 cells
666 cultured in the absence (A, C, E) or presence (B, D, F) of Fog. (A-B') non-transfected
667 S2 cells. (C-D') Mist-transfected S2 cells. (E-F') Smog-transfected S2 cells. A-F, phase
668 contrast; A'-F', merged images of phase contrast and V5 signals for transfected cells
669 (green). White arrowhead in E', Smog- transfected S2 cell is not contracting in the
670 absence of Fog. Magenta arrowheads, contracting cells. (G) Quantification of
671 percentage of contracting cells. n=~100 cells per condition from three independent
672 experiments. ****p≤0.0001 (Two-way ANOVA with Tukey's multiple comparison post
673 hoc analysis).
674
675 **Figure 3. *smog* knockdown and loss result in apical constriction defects in the SG**
676 **and disrupted epithelial morphology.** (A-F) Confocal images of SGs in control (A),
677 with zygotic knockdown of *smog* by using *TRiP.HMC03192* (B), with M/Z knockdown of
678 *smog* by using *TRiP.GL01473* (C), WT (D), *smog* null [mild] (E), and *smog* null [severe]
679 (F). (A'-F') Cell segmentation based on apical areas of A-F. Red and white lines, SG
680 boundary. Asterisks, invagination pit. (G, H) Quantification of percentage (left) and
681 cumulative percentage (right) of cells with different apical areas. Mann-Whitney U test
682 (for percentage of cells) and Kolmogorov-Smirnov test (for cumulative percentage of
683 cells). n=8 SGs (control, 902 cells; *smog* RNAi (Z), 823 cells; *smog* RNAi (M/Z), 881
684 cells; WT, 892 cells; *smog* null [mild], 859 cells); 6 SGs (*smog* null [severe], 672 cells).
685 ***p<0.001; ****p<0.0001. (I-L) 3D reconstruction of confocal z-sections of SGs using
686 Imaris for WT (I), M/Z knockdown of *smog* (J), *smog* null [mild] (K), and *smog* null
687 [severe] (L). Green, E-Cad. Magenta, CrebA. Asterisks, invagination pit. Arrows in J and
688 L, exaggerated grooves. Arrowheads in J and L, enlarged SG cells. (M, N) Tile scan
689 confocal images of stage 11 embryos in WT (M) and M/Z knockdown of *smog* (N).
690 Green, E-Cad. Magenta, CrebA. Arrows, ventral midline. Arrowheads, SG.
691
692 **Figure 4. *smog* regulates all three pools of myosin in the SG in a Fog-dependent**
693 **and -independent manner.** (A-D'') Confocal images of SGs with sqh-GFP (green) and
694 E-Cad (magenta) signals. Compared to control (A-A''), sqh-GFP signals are dispersed
695 in SGs with zygotic (B-B'') and M/Z (C-C'') knockdown of *smog* and in *smog* null [mild]

embryos (D-D''). (A'-D'') Higher magnification of the yellow boxed region in A-D. (E-H'') Confocal images of SGs with Rok-GFP (green) and E-Cad (magenta) signals. Compared to control (E-E''), Rok-GFP signals are dispersed in SGs with zygotic (F-F'') and M/Z (G-G'') knockdown of *smog* and in *smog* null [mild] embryos (H-H''). (E'-H") Magnified images of the yellow boxed region in E-H. (I-L) Quantification of apicomedial myosin intensity (I), junctional myosin intensity (J), area of apicomedial myosin particles (K), and area of Rok-GFP particles (L). *p≤0.05; **p≤0.01; ***p≤0.001; ****p≤0.0001 (Welch's t-test). n=5 SGs, 100 cells (I-K) and 5 SGs, 75 cells (L) for each genotype. (M) Control SG with high myosin intensity at the placode boundary (arrowheads in insets in M, M''). (N) *smog* null [severe] SGs have low myosin intensity. Arrowheads in insets in N, N'', discontinuous myosin at the SG boundary. (O) Analysis of the circularity of the SG placode boundary as a measure of smoothness and tension. An example of a WT SG stained for E-Cad (magenta) and sqh-GFP (green) with the boundaries measured. Red line, SG boundary; gray line, cell boundary one cell row outside the SG boundary; blue line, cell boundary one cell row inside the SG boundary. (P) Quantification of circularity of the SG, outer, and inner boundary in control and *smog* null [severe] SGs. Asterisks, invagination pit. *p≤0.05; **p≤0.01; ***p≤0.001 (Welch's t-test). n=5 SGs for each genotype.

Figure 5. Smog is required for maintaining epithelial integrity and the microtubule networks. (A-D) Confocal images of stage 11 WT (A, C) and *smog* null [severe] (B, D) embryos (A, B) Embryos stained for E-Cad (green) and CrebA (magenta). (A', B') Magnified view of the white boxed region in A and B. Compared to uniform and continuous E-Cad signals in WT embryonic epithelial cells (A'), E-Cad signals are absent in regions of epithelial cells in *smog* mutants (arrowheads in B'). (C, D) Embryos stained for Crb (green) and CrebA (magenta). (C', D') magnified view of the white box region in C and D. In contrast to continuous WT Crb signals (C'), Crb is almost absent in regions of epithelial cells in *smog* mutants (arrowheads in D'). (E-J) E-Cad (E-G) and Crb (H-J) signals in WT (E, H), *smog* null [mild] (F, I), and *smog* null [severe] (G, J) embryos. Insets, magnified view of yellow boxed region in the SG. Arrowheads, gaps in E-Cad or Crb signals. (K-N) Quantification of the number of gaps in E-Cad (K) and Crb

727 (M) signals and the ratio of gap length to total junctional length for E-Cad (L) and Crb
728 (N). n=5 SGs, 50 cells per genotype. **p≤0.01; ***p≤0.001 (Welch's t-test). (O-R)
729 Compared to WT (O, Q), acetylated tubulin signals are almost absent in the SG in *smog*
730 mutants (P), and tyrosinated tubulin signals are also reduced in *smog* mutants (R). Red
731 dotted lines, SG boundary. (S) Quantification of the ratio of tyrosinated tubulin intensity
732 in SG cells to the intensity in cells outside the SG placode. n=4 SGs (control); 5 SGs
733 (*smog* null). *p≤0.05 (Welch's t-test). Asterisks, invagination pit.

734

735 **Figure 6. Smog is required for maintaining cortical actin networks during SG**
736 **invagination.** (A-B''') Rok-GFP (green) and E-Cad (magenta) in SGs in control (A-A''')
737 and *smog* null [severe] (B-B''') embryos. (A'-B'') Higher magnification of the white boxed
738 regions in A and B. (A''', B''') x-z sections across the yellow lines in A and B. Red
739 arrowheads, normal Rok-GFP signals accumulated in the apicomedial region of control
740 SG cells. White arrowheads, blebs in SG cells in *smog* mutants enriched with Rok-GFP
741 signals. (C, D) SGs stained for Dia (green) and phalloidin (magenta) in WT (C) and
742 *smog* null mutant (D) embryos. Compared to high intensity of Dia (red arrowheads in C,
743 C'') and phalloidin (cyan arrowheads in D, D'') in the WT SG, Dia and phalloidin signals
744 are reduced in SGs in *smog* null mutants (red and cyan arrowheads in D-D''). (E-G)
745 Quantification of Dia intensity in apicomedial (E) and junctional (F) regions and the ratio
746 of apicomedial to junctional Dia intensity (G). (H-I'') Rok-GFP (green) and E-Cad
747 (magenta) in *chic* RNAi in the wild-type (H-H'') and *smog* mutant background (I-I''). (H'-
748 I'') Higher magnification of the white boxed regions in H, I. In *chic* RNAi SGs, Rok-GFP
749 signals accumulate in the apicomedial region of SG cells (red arrowheads in H' and H'').
750 *smog* null [mild] SG cells with *chic* knockdown show membrane blebs with enriched
751 Rok-GFP signals (white arrowheads in I' and I''). Asterisks, invagination pit. *p≤0.05;
752 **p≤0.01 (Welch's t-test). n=5 SGs, 50 cells for each genotype.

753

754 **Figure 7. A proposed model for roles of Smog during epithelial tube formation.**
755 During SG invagination, Smog responds to Fog signal to promote Rok accumulation
756 and apicomedial myosin formation to control apical constriction (red arrows).
757 Independent of Fog (and responding to an as-yet-unknown ligand X), Smog regulates

758 epithelial integrity by regulating junctional and the supracellular myosin pools, the
759 microtubule networks, and key apical/junctional components (grey arrows). Smog is
760 also required for cortical actin organization during SG invagination, through regulating
761 Dia levels (grey arrows). Different ligands may recruit specific G proteins and RhoGEFs
762 to activate distinct downstream effectors.
763
764 **Supplementary Figure S1. *smog* knockdown using a weaker RNAi line also shows**
765 **apical constriction defects in SG cells.** (A, A') A representative confocal image (A) of
766 the stage 11 SG in *fog* mutants and the corresponding heat map of apical areas (A').
767 The embryo surface is often uneven in *fog* mutant embryos due to additional folding and
768 grooves, resulting in some cells outside the SG being out of focus and not shown in the
769 image. (B-C') Confocal images of SGs in control (B) and zygotic knockdown of *smog* by
770 using *TRiP.GL01473* (C) and corresponding heat maps of apical areas (B' and C'). Red
771 and white lines, SG boundary. Asterisks, invagination pit. (D) Quantification of
772 percentage and cumulative percentage of cells with different apical areas. Mann-
773 Whitney U test (for percentage of cells) and Kolmogorov-Smirnov test (for cumulative
774 percentage of cells). n=8 SGs (control, 902 cells; *smog* RNAi (Z), 856 cells). **p≤0.01.
775
776 **Supplementary Figure S2. SGs in *smog* null mutants have relatively normal**
777 **morphology at stage 14 and later during embryogenesis.** (A, B) Confocal images of
778 stage 15 WT (A) and *smog* null embryos stained for E-Cad (green) and CrebA
779 (magenta). (C-G) SGs stained for E-Cad in WT (C, E), *smog* M/Z knockdown (F), and
780 *smog* null mutant (D, G) embryos. All embryos at stage 14 and later have relatively
781 normal morphology, including the SG, except for a rare case of the crooked SG in *smog*
782 null mutants (D).
783
784 **Supplementary Figure S3. *smog* loss leads to the reduction of Crb levels in the**
785 **whole embryo and loss of Crb anisotropy at the SG boundary.** (A, B) Confocal
786 images of stage 14 WT (A) and *smog* null [severe] mutant (B) embryos stained for Crb
787 (green) and CrebA (magenta). (A', B') Magnified view of the white boxed region in A and
788 B. Compared to clear Crb signals at the cell boundary in WT (A'), Crb levels are

789 reduced and diffused in some *smog* null mutant embryos with a severely defective
790 morphology (B'). (C-H''') control (C-E''') and *smog* null [severe] embryos (F-H''')
791 showing sqh-mCh (green) and Crb (magenta) signals. (D, G) Cells at the SG boundary.
792 (E, H) SG cells near the invagination pit (asterisk). (D'-H''') Higher magnification of the
793 boxed regions. In contrast to high myosin (red arrowheads in D''') and low Crb (cyan
794 arrowheads in D'') levels in the SG boundary in control embryos, the overall Crb levels
795 are reduced in *smog* null embryos, showing loss of anisotropic localization of Crb at the
796 SG boundary (G-H''').
797
798 **Supplementary Figure S4. *smog* loss leads to bleb formation in SG cells as well**
799 **as outside the SG placode.** (A-C'') Confocal images for Rok-GFP (green) and E-Cad
800 (magenta) signals in stage 11 SGs in control (A-A''), *smog* null [mild] (B-B''), and *fog*
801 mutant (C-C'') embryos. Blebs are not observed in these embryos. Due to the uneven
802 embryo surface in *fog* mutants, apical/junctional and more basal regions are shown for
803 SG cells near and far from the invagination pit, respectively, in the single z section. (D-
804 E'') Confocal images for Rok-GFP signals in control (D-D'') and *smog* null [severe] (E-
805 E'') embryos. Blebs are observed both in non-SG cells outside the SG placode (red
806 arrowheads in E') and SG cells (cyan arrowheads in E''). Yellow arrowheads in D'',
807 normal Rok accumulation in the apicomedial region of SG cells. Asterisk, invagination
808 pit.

809 **References**

810 **Abreu-Blanco, M. T., Verboon, J. M. and Parkhurst, S. M.** (2014). Coordination of
811 Rho Family GTPase Activities to Orchestrate Cytoskeleton Responses during Cell
812 Wound Repair. *Current Biology* **24**, 144–155.

813 **Afshar, K., Stuart, B. and Wasserman, S. A.** (2000). Functional analysis of the
814 Drosophila diaphanous FH protein in early embryonic development. *Development*
815 *(Cambridge, England)* **127**, 1887–97.

816 **Andrew, D. J. and Ewald, A. J.** (2010). Morphogenesis of epithelial tubes: Insights into
817 tube formation, elongation, and elaboration. *Developmental Biology* **341**, 34–55.

818 **Aoki, K., Maeda, F., Nagasako, T., Mochizuki, Y., Uchida, S. and Ikenouchi, J.**
819 (2016). A RhoA and Rnd3 cycle regulates actin reassembly during membrane
820 blebbing. *Proceedings of the National Academy of Sciences* **113**, E1863–E1871.

821 **Barrett, K., Leptin, M. and Settleman, J.** (1997). The Rho GTPase and a Putative
822 RhoGEF Mediate a Signaling Pathway for the Cell Shape Changes in Drosophila
823 Gastrulation. *Cell* **91**, 905–915.

824 **Benton, M. A., Frey, N., Nunes da Fonseca, R., von Levetzow, C., Stappert, D.,**
825 **Hakeemi, M. S., Conrads, K. H., Pechmann, M., Panfilio, K. A., Lynch, J. A., et**
826 **al.** (2019). Fog signaling has diverse roles in epithelial morphogenesis in insects.
827 *eLife* **8**, e47346.

828 **Blanchard, G. B., Murugesu, S., Adams, R. J., Martinez-Arias, A. and Gorfinkiel, N.**
829 (2010). Cytoskeletal dynamics and supracellular organisation of cell shape
830 fluctuations during dorsal closure. *Development* **137**, 2743–2752.

831 **Booth, A. J. R., Blanchard, G. B., Adams, R. J. and Röper, K.** (2014). A Dynamic
832 Microtubule Cytoskeleton Directs Medial Actomyosin Function during Tube
833 Formation. *Developmental Cell* **29**, 562–576.

834 **Charras, G. T.** (2008). A short history of blebbing. *Journal of Microscopy* **231**, 466–478.

835 **Charras, G. T., Yarrow, J. C., Horton, M. A., Mahadevan, L. and Mitchison, T. J.**
836 (2005). Non-equilibration of hydrostatic pressure in blebbing cells. *Nature* **435**, 365–
837 369.

838 **Chung, S., Hanlon, C. D. and Andrew, D. J.** (2014). Building and specializing
839 epithelial tubular organs: the Drosophila salivary gland as a model system for

840 revealing how epithelial organs are specified, form and specialize. *WIREs Dev Biol*
841 **3**, 281–300.
842 **Chung, S., Kim, S. and Andrew, D. J.** (2017). Uncoupling apical constriction from
843 tissue invagination. *eLife* **6**, e22235.
844 **Cooley, L., Verheyen, E. and Ayers, K.** (1992). chickadee encodes a profilin required
845 for intercellular cytoplasm transport during Drosophila oogenesis. *Cell* **69**, 173–184.
846 **Costa, M., Wilson, E. T. and Wieschaus, E.** (1994). A putative cell signal encoded by
847 the folded gastrulation gene coordinates cell shape changes during Drosophila
848 gastrulation. *Cell* **76**, 1075–1089.
849 **Dawes-Hoang, R. E., Parmar, K. M., Christiansen, A. E., Phelps, C. B., Brand, A. H.**
850 **and Wieschaus, E. F.** (2005). *folded gastrulation* , cell shape change and the
851 control of myosin localization. *Development* **132**, 4165–4178.
852 **Fox, D. T. and Peifer, M.** (2007). Abelson kinase (Abl) and RhoGEF2 regulate actin
853 organization during cell constriction in *Drosophila*. *Development* **134**, 567–578.
854 **Garcia De Las Bayonas, A., Philippe, J. M., Lellouch, A. C. and Lecuit, T.** (2019).
855 Distinct RhoGEFs Activate Apical and Junctional Contractility under Control of G
856 Proteins during Epithelial Morphogenesis. *Current Biology* **29**, 3370-3385.e7.
857 **Girdler, G. C. and Röper, K.** (2014). Controlling cell shape changes during salivary
858 gland tube formation in Drosophila. *Seminars in Cell & Developmental Biology* **31**,
859 74–81.
860 **Goode, B. L. and Eck, M. J.** (2007). Mechanism and Function of Formins in the Control
861 of Actin Assembly. *Annual Review of Biochemistry* **76**, 593–627.
862 **Gorfinkiel, N. and Blanchard, G. B.** (2011). Dynamics of actomyosin contractile
863 activity during epithelial morphogenesis. *Current Opinion in Cell Biology* **23**, 531–
864 539.
865 **Guglielmi, G., Barry, J. D., Huber, W. and de Renzis, S.** (2015). An Optogenetic
866 Method to Modulate Cell Contractility during Tissue Morphogenesis. *Developmental*
867 *cell* **35**, 646–660.
868 **Häcker, U. and Perrimon, N.** (1998). *DRhoGEF2* encodes a member of the Dbl family
869 of oncogenes and controls cell shape changes during gastrulation in *Drosophila*.
870 *Genes & Development* **12**, 274–284.

871 **Henderson, K. D. and Andrew, D. J.** (2000). Regulation and Function of Scr, exd, and
872 hth in the Drosophila Salivary Gland. *Developmental Biology* **217**, 362–374.
873 **Homem, C. C. F. and Peifer, M.** (2008). Diaphanous regulates myosin and adherens
874 junctions to control cell contractility and protrusive behavior during morphogenesis.
875 *Development* **135**, 1005–1018.
876 **Izquierdo, E., Quinkler, T. and de Renzis, S.** (2018). Guided morphogenesis through
877 optogenetic activation of Rho signalling during early Drosophila embryogenesis.
878 *Nature Communications* **9**, 2366.
879 **Jha, A., van Zanten, T. S., Philippe, J.-M., Mayor, S. and Lecuit, T.** (2018).
880 Quantitative Control of GPCR Organization and Signaling by Endocytosis in
881 Epithelial Morphogenesis. *Current Biology* **28**, 1570-1584.e6.
882 **Jodoin, J. N., Coravos, J. S., Chanet, S., Vasquez, C. G., Tworoger, M., Kingston,**
883 **E. R., Perkins, L. A., Perrimon, N. and Martin, A. C.** (2015). Stable Force Balance
884 between Epithelial Cells Arises from F-Actin Turnover. *Developmental Cell* **35**, 685–
885 697.
886 **Kanesaki, T., Hirose, S., Grosshans, J. and Fuse, N.** (2013). Heterotrimeric G protein
887 signaling governs the cortical stability during apical constriction in Drosophila
888 gastrulation. *Mechanisms of Development* **130**, 132–142.
889 **Kerridge, S., Munjal, A., Philippe, J.-M., Jha, A., de las Bayonas, A. G., Saurin, A.**
890 **J. and Lecuit, T.** (2016). Modular activation of Rho1 by GPCR signalling imparts
891 polarized myosin II activation during morphogenesis. *Nature Cell Biology* **18**, 261–
892 270.
893 **Kim, H. Y., Varner, V. D. and Nelson, C. M.** (2013). Apical constriction initiates new
894 bud formation during monopodial branching of the embryonic chicken lung.
895 *Development* **140**, 3146–3155.
896 **Knirr, S., Azpiazu, N. and Frasch, M.** (1999). The role of the NK-homeobox gene
897 slouch (S59) in somatic muscle patterning. *Development (Cambridge, England)* **126**,
898 4525–35.
899 **Ko, C. S., Tserunyan, V. and Martin, A. C.** (2019). Microtubules promote intercellular
900 contractile force transmission during tissue folding. *Journal of Cell Biology* **218**,
901 2726–2742.

902 **Kölsch, V., Seher, T., Fernandez-Ballester, G. J., Serrano, L. and Leptin, M.** (2007).
903 Control of *Drosophila* Gastrulation by Apical Localization of Adherens Junctions and
904 RhoGEF2. *Science* **315**, 384–386.
905 **Le, T. P. and Chung, S.** (2021). Regulation of apical constriction via microtubule- and
906 Rab11-dependent apical transport during tissue invagination. *Molecular Biology of*
907 *the Cell* **32**, 1033–1047.
908 **le Droguen, P.-M., Claret, S., Guichet, A. and Brodu, V.** (2015). Microtubule-
909 dependent apical restriction of recycling endosomes sustains adherens junctions
910 during morphogenesis of the *Drosophila* tracheal system. *Development* **142**, 363–
911 374.
912 **Levayer, R. and Lecuit, T.** (2012). Biomechanical regulation of contractility: spatial
913 control and dynamics. *Trends in cell biology* **22**, 61–81.
914 **Lord, S. J., Velle, K. B., Mullins, R. D. and Fritz-Laylin, L. K.** (2020). SuperPlots:
915 Communicating reproducibility and variability in cell biology. *Journal of Cell Biology*
916 **219**, e202001064.
917 **Lubarsky, B. and Krasnow, M. A.** (2003). Tube morphogenesis: making and shaping
918 biological tubes. *Cell* **112**, 19–28.
919 **Manning, A. J. and Rogers, S. L.** (2014). The Fog signaling pathway: Insights into
920 signaling in morphogenesis. *Developmental Biology* **394**, 6–14.
921 **Manning, A. J., Peters, K. A., Peifer, M. and Rogers, S. L.** (2013). Regulation of
922 Epithelial Morphogenesis by the G Protein–Coupled Receptor Mist and Its Ligand
923 Fog. *Science Signaling* **6**, ra98.
924 **Martin, A. C. and Goldstein, B.** (2014). Apical constriction: themes and variations on a
925 cellular mechanism driving morphogenesis. *Development* **141**, 1987–1998.
926 **Martin, A. C., Kaschube, M. and Wieschaus, E. F.** (2009). Pulsed contractions of an
927 actin–myosin network drive apical constriction. *Nature* **457**, 495–499.
928 **Mason, F. M., Tworoger, M. and Martin, A. C.** (2013). Apical domain polarization
929 localizes actin–myosin activity to drive ratchet-like apical constriction. *Nature Cell*
930 *Biology* **15**, 926–936.

931 **Massarwa, R., Schejter, E. D. and Shilo, B.-Z.** (2009). Apical Secretion in Epithelial
932 Tubes of the Drosophila Embryo Is Directed by the Formin-Family Protein
933 Diaphanous. *Developmental Cell* **16**, 877–888.
934 **Munjal, A. and Lecuit, T.** (2014). Actomyosin networks and tissue morphogenesis.
935 *Development (Cambridge, England)* **141**, 1789–93.
936 **Myat, M. M. and Andrew, D. J.** (2000). Organ shape in the Drosophila salivary gland is
937 controlled by regulated, sequential internalization of the primordia. *Development*
938 *(Cambridge, England)* **127**, 679–91.
939 **Nikolaidou, K. K. and Barrett, K.** (2004). A Rho GTPase Signaling Pathway Is Used
940 Reiteratively in Epithelial Folding and Potentially Selects the Outcome of Rho
941 Activation. *Current Biology* **14**, 1822–1826.
942 **Parks, S. and Wieschaus, E.** (1991). The drosophila gastrulation gene concertina
943 encodes a Gα-like protein. *Cell* **64**, 447–458.
944 **Plageman, T. F., Chauhan, B. K., Yang, C., Jaudon, F., Shang, X., Zheng, Y., Lou,**
945 **M., Debant, A., Hildebrand, J. D. and Lang, R. A.** (2011). A Trio-RhoA-Shroom3
946 pathway is required for apical constriction and epithelial invagination. *Development*
947 **138**, 5177–5188.
948 **Rao, M. V. and Zaidel-Bar, R.** (2016). Formin-mediated actin polymerization at cell–cell
949 junctions stabilizes E-cadherin and maintains monolayer integrity during wound
950 repair. *Molecular Biology of the Cell* **27**, 2844–2856.
951 **Romero, S., le Clainche, C., Didry, D., Egile, C., Pantaloni, D. and Carlier, M.-F.**
952 (2004). Formin Is a Processive Motor that Requires Profilin to Accelerate Actin
953 Assembly and Associated ATP Hydrolysis. *Cell* **119**, 419–429.
954 **Röper, K.** (2012). Anisotropy of Crumbs and aPKC Drives Myosin Cable Assembly
955 during Tube Formation. *Developmental Cell* **23**, 939–953.
956 **Rousso, T., Shewan, A. M., Mostov, K. E., Schejter, E. D. and Shilo, B.-Z.** (2013).
957 Apical targeting of the formin Diaphanous in Drosophila tubular epithelia. *eLife* **2**, 1–
958 19.
959 **Royou, A., Field, C., Sisson, J. C., Sullivan, W. and Karess, R.** (2004). Reassessing
960 the Role and Dynamics of Nonmuscle Myosin II during Furrow Formation in Early
961 *Drosophila* Embryos. *Molecular Biology of the Cell* **15**, 838–850.

962 **Sanchez-Corrales, Y. E., Blanchard, G. B. and Röper, K.** (2018). Radially patterned
963 cell behaviours during tube budding from an epithelium. *eLife* **7**, e35717.
964 **Shewan, A. M., Maddugoda, M., Kraemer, A., Stehbens, S. J., Verma, S., Kovacs,**
965 **E. M. and Yap, A. S.** (2005). Myosin 2 Is a Key Rho Kinase Target Necessary for
966 the Local Concentration of E-Cadherin at Cell–Cell Contacts. *Molecular Biology of*
967 *the Cell* **16**, 4531–4542.
968 **Sidor, C., Stevens, T. J., Jin, L., Boulanger, J. and Röper, K.** (2020). Rho-Kinase
969 Planar Polarization at Tissue Boundaries Depends on Phospho-regulation of
970 Membrane Residence Time. *Developmental Cell* **52**, 364-378.e7.
971 **Sweeton, D., Parks, S., Costa, M. and Wieschaus, E.** (1991). Gastrulation in
972 Drosophila: the formation of the ventral furrow and posterior midgut invaginations.
973 *Development (Cambridge, England)* **112**, 775–89.
974 **Vázquez-Victorio, G., González-Espinosa, C., Espinosa-Riquer, Z. P. and Macías-**
975 **Silva, M.** (2016). GPCRs and actin–cytoskeleton dynamics. *Methods in Cell Biology*
976 **132**, 165–188.
977 **Weng, M. and Wieschaus, E.** (2016). Myosin-dependent remodeling of adherens
978 junctions protects junctions from Snail-dependent disassembly. *Journal of Cell*
979 *Biology* **212**, 219–229.
980 **Westermann, S. and Weber, K.** (2003). Post-translational modifications regulate
981 microtubule function. *Nature Reviews Molecular Cell Biology* **4**, 938–948.
982 **Zweifel, M. E. and Courtemanche, N.** (2020). Profilin's Affinity for Formin Regulates
983 the Availability of Filament Ends for Actin Monomer Binding. *Journal of Molecular*
984 *Biology* **432**, 166688.
985

Figure 1.

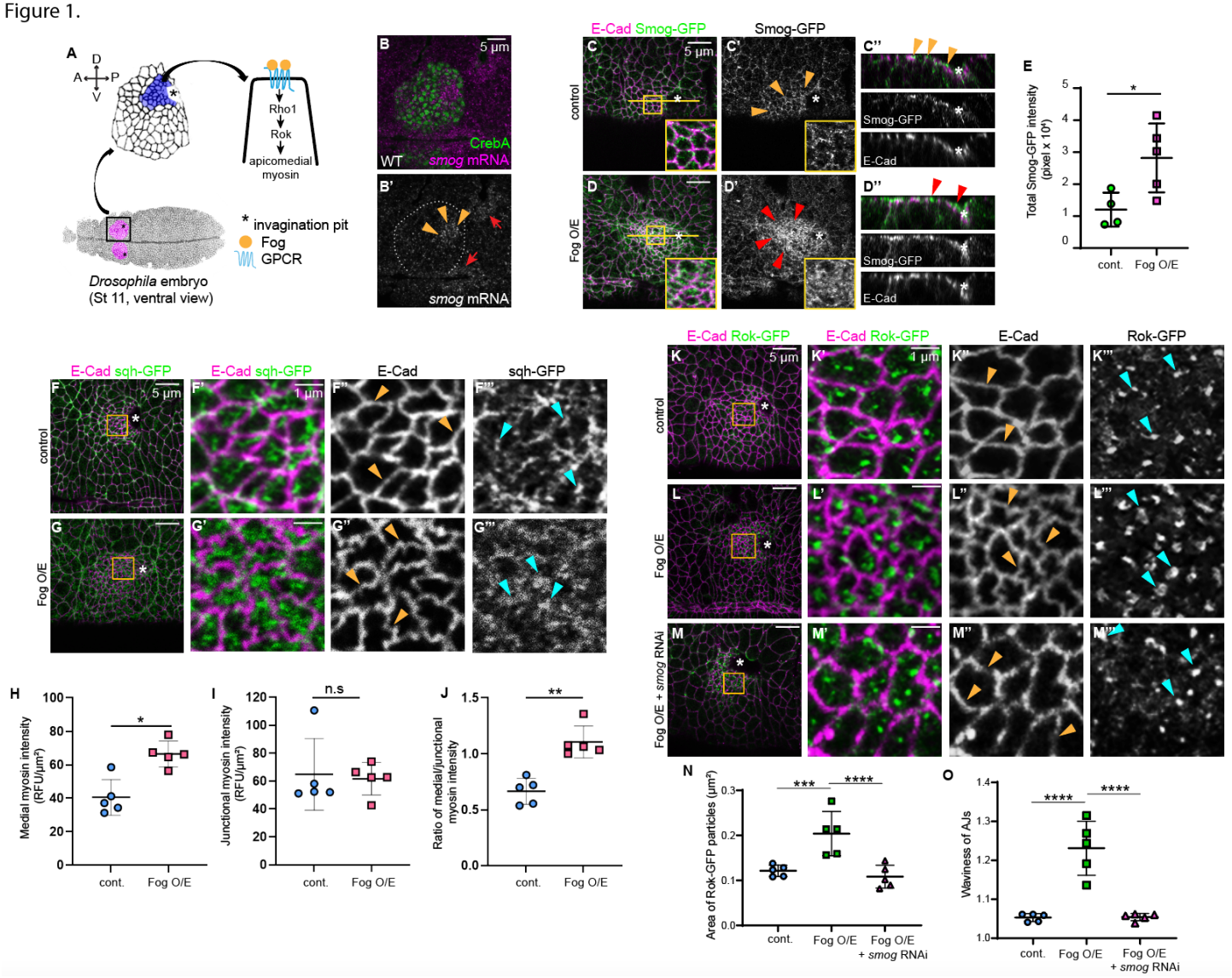
A
D
A
P
V
Rho1
Rok
apicomedial myosin
* invagination pit
Fog
GPCR
Drosophila embryo
(St 11, ventral view)
B
5 µm
CrebA
WT
smog mRNA
B'
smog mRNA
E-Cad Smog-GFP
Smog-GFP
control
Fog O/E
C
C'
C''
D
D'
D''
Smog-GFP
E-Cad
E
Total Smog-GFP intensity (pixel x 10⁴)
cont.
Fog O/E
E-Cad sqh-GFP
E-Cad
sqh-GFP
F
F'
F''
F'''
G
G'
G''
G'''
1 µm
H
Medial myosin intensity (RFU/µm²)
I
Junctional myosin intensity (RFU/µm²)
n.s
J
Ratio of medial/junctional myosin intensity
E-Cad Rok-GFP
Rok-GFP
K
K'
K''
K'''
L
L'
L''
L'''
M
M'
M''
M'''
Fog O/E + smog RNAi
N
Area of Rok-GFP particles (µm²)
Fog O/E + smog RNAi
O
Waviness of AJs

Figure 2.

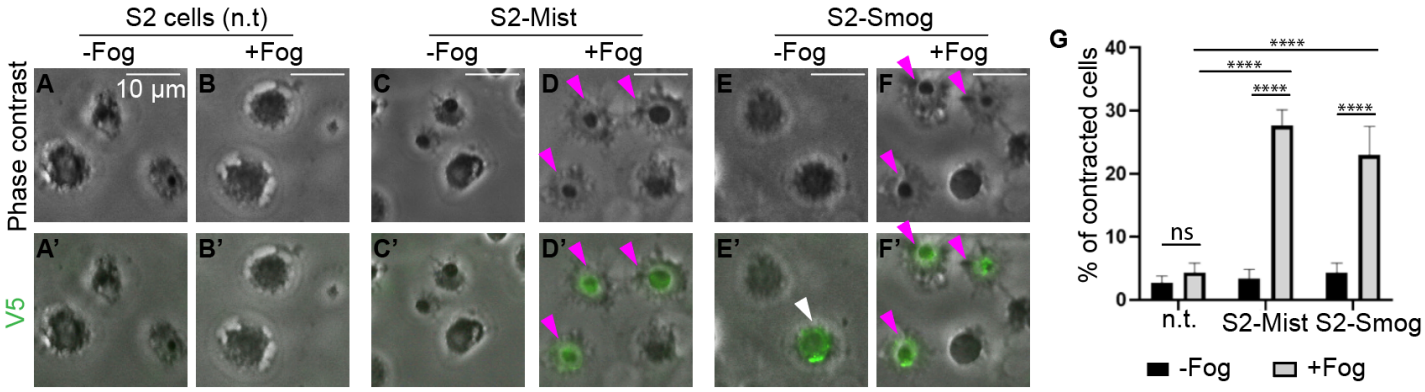
S2 cells (n.t)
S2-Mist
S2-Smog
-Fog
+Fog
Phase contrast
V5
10 µm
A
B
C
D
E
F
A'
B'
C'
D'
E'
F'
G
% of contracted cells
40
30
20
10
0
ns
****
n.t.
S2-Mist
S2-Smog
-Fog
+Fog

Figure 3.

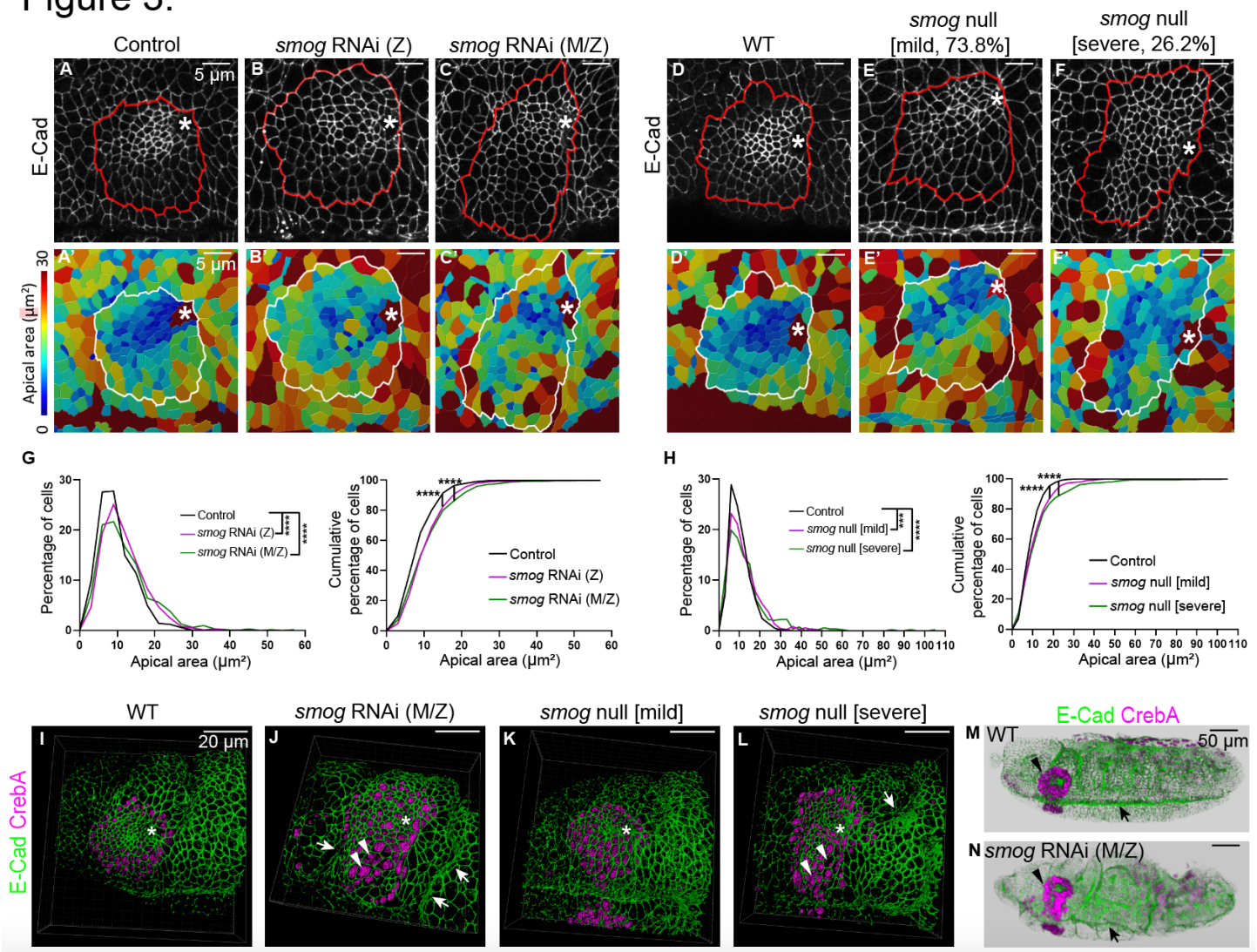
Control
smog RNAi (Z)
smog RNAi (M/Z)
WT
smog null [mild, 73.8%]
smog null [severe, 26.2%]
E-Cad
5 µm
Apical area (µm²)
G
H
Percentage of cells
Cumulative percentage of cells
Apical area (µm²)
Control
smog RNAi (Z)
smog RNAi (M/Z)
smog null [mild]
smog null [severe]
WT
smog RNAi (M/Z)
smog null [mild]
smog null [severe]
E-Cad CrebA
20 µm
50 µm

Figure 4.

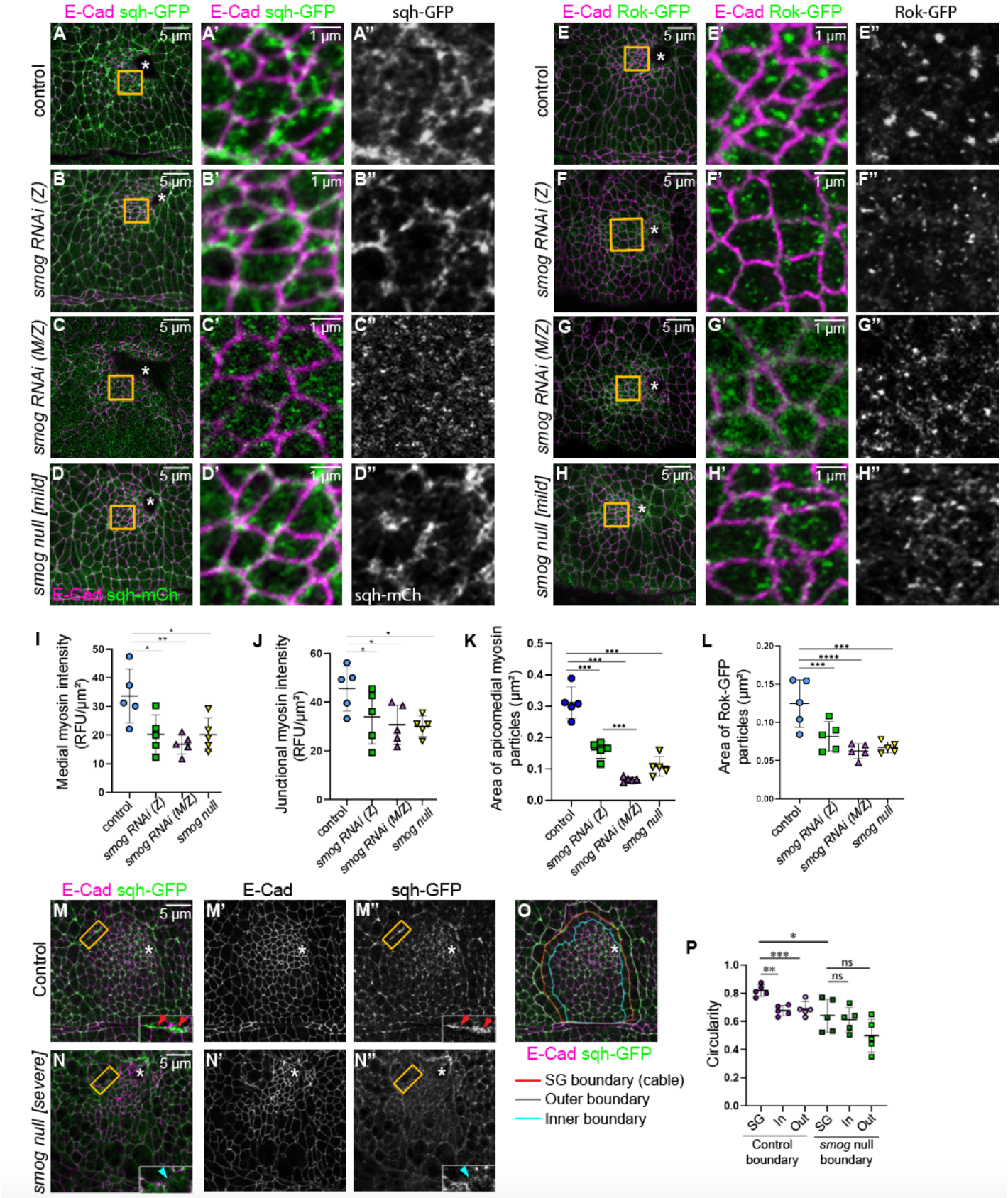
E-Cad sqh-GFP
E-Cad sqh-GFP
sqh-GFP
E-Cad Rok-GFP
E-Cad Rok-GFP
Rok-GFP
control
smog RNAi (Z)
smog RNAi (M/Z)
smog null [mild]
5 µm
1 µm
E-Cad sqh-mCh
sqh-mCh
Medial myosin intensity (RFU/µm²)
Junctional myosin intensity (RFU/µm²)
Area of apicomedial myosin particles (µm²)
Area of Rok-GFP particles (µm²)
control
smog RNAi (Z)
smog RNAi (M/Z)
smog null
E-Cad sqh-GFP
E-Cad
sqh-GFP
Control
smog null [severe]
E-Cad sqh-GFP
SG boundary (cable)
Outer boundary
Inner boundary
Circularity
SG
In
Out
Control boundary
smog null boundary
ns

Figure 5.

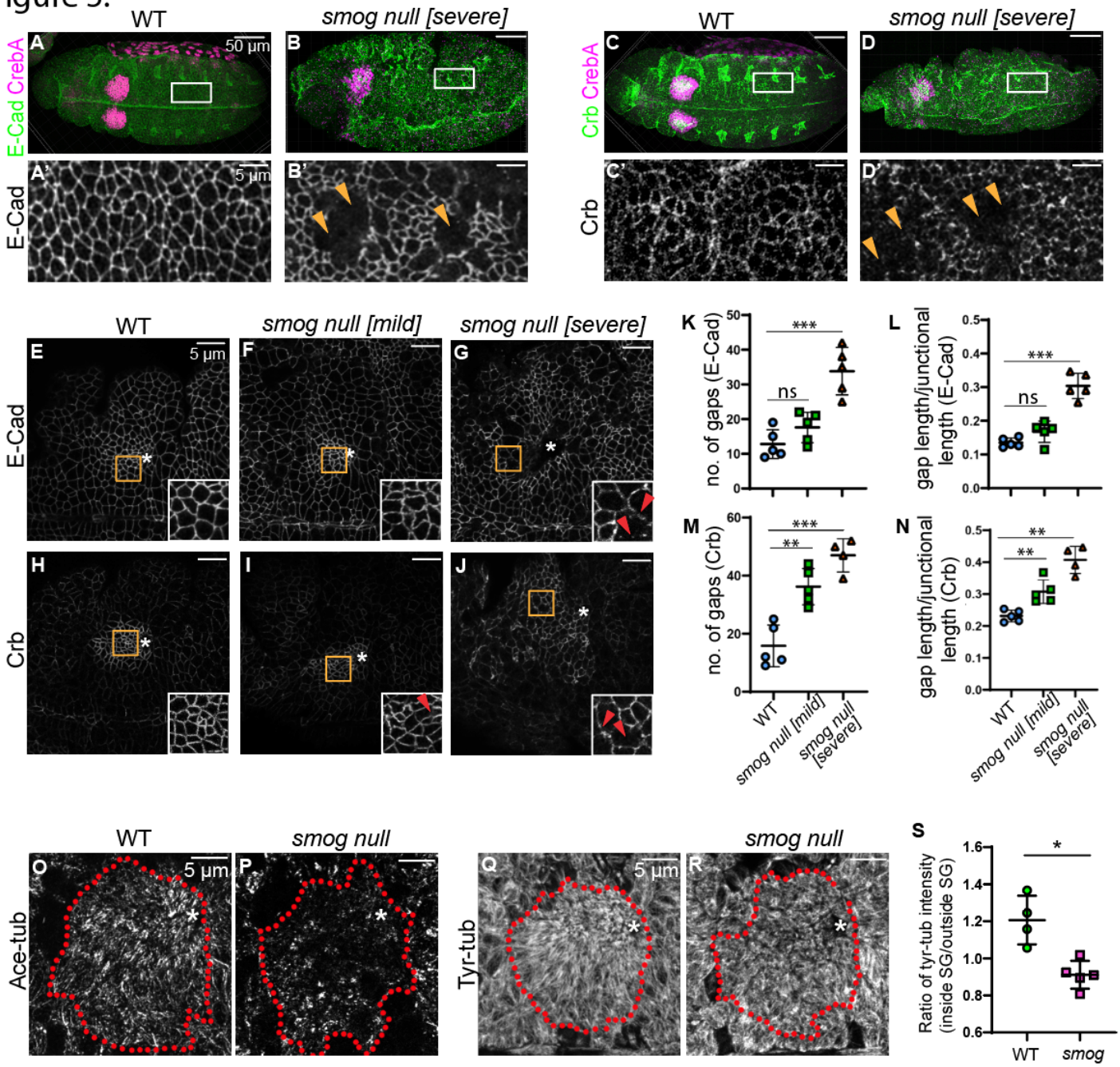
WT
smog null [severe]
E-Cad CrebA
A
50 µm
B
A'
5 µm
B'
E-Cad
WT
smog null [severe]
Crb CrebA
C
D
C'
D'
Crb
WT
smog null [mild]
smog null [severe]
E
5 µm
F
G
E-Cad
H
I
J
Crb
K
no. of gaps (E-Cad)
***
ns
L
gap length/junctional length (E-Cad)
***
ns
M
no. of gaps (Crb)
***
**
N
gap length/junctional length (Crb)
**
**
WT
smog null [mild]
smog null [severe]
WT
smog null
O
5 µm
P
Ace-tub
Q
5 µm
R
Tyr-tub
S
Ratio of tyr-tub intensity (inside SG/outside SG)
*
WT
smog

Figure 6.

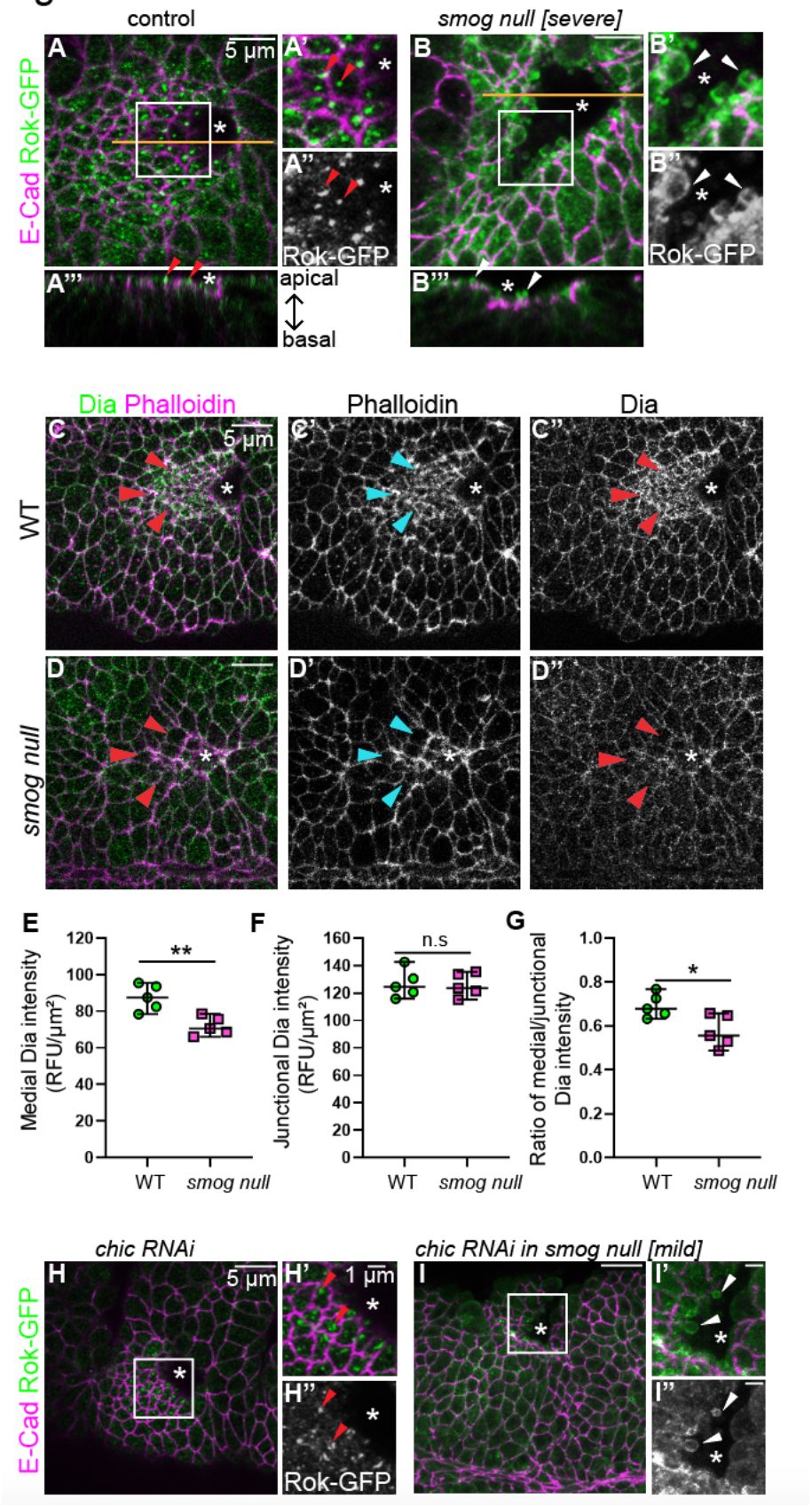
control
smog null [severe]
E-Cad Rok-GFP
5 µm
Rok-GFP
apical
basal
Dia Phalloidin
Phalloidin
Dia
WT
smog null
E
F
G
Medial Dia intensity (RFU/µm²)
Junctional Dia intensity (RFU/µm²)
Ratio of medial/junctional Dia intensity
**
n.s
*
WT
smog null
chic RNAi
chic RNAi in smog null [mild]
1 µm

Figure 7.

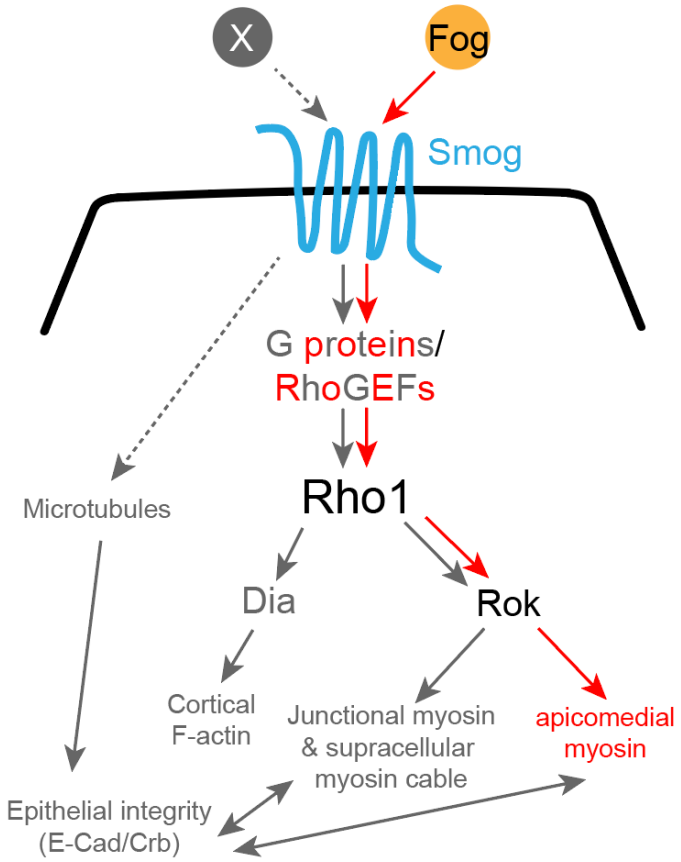
X
Fog
Smog
G proteins/
RhoGEFs
Microtubules
Rho1
Dia
Rok
Cortical
F-actin
Junctional myosin
& supracellular
myosin cable
apicomedial
myosin
Epithelial integrity
(E-Cad/Crb)

Sup Fig. S1

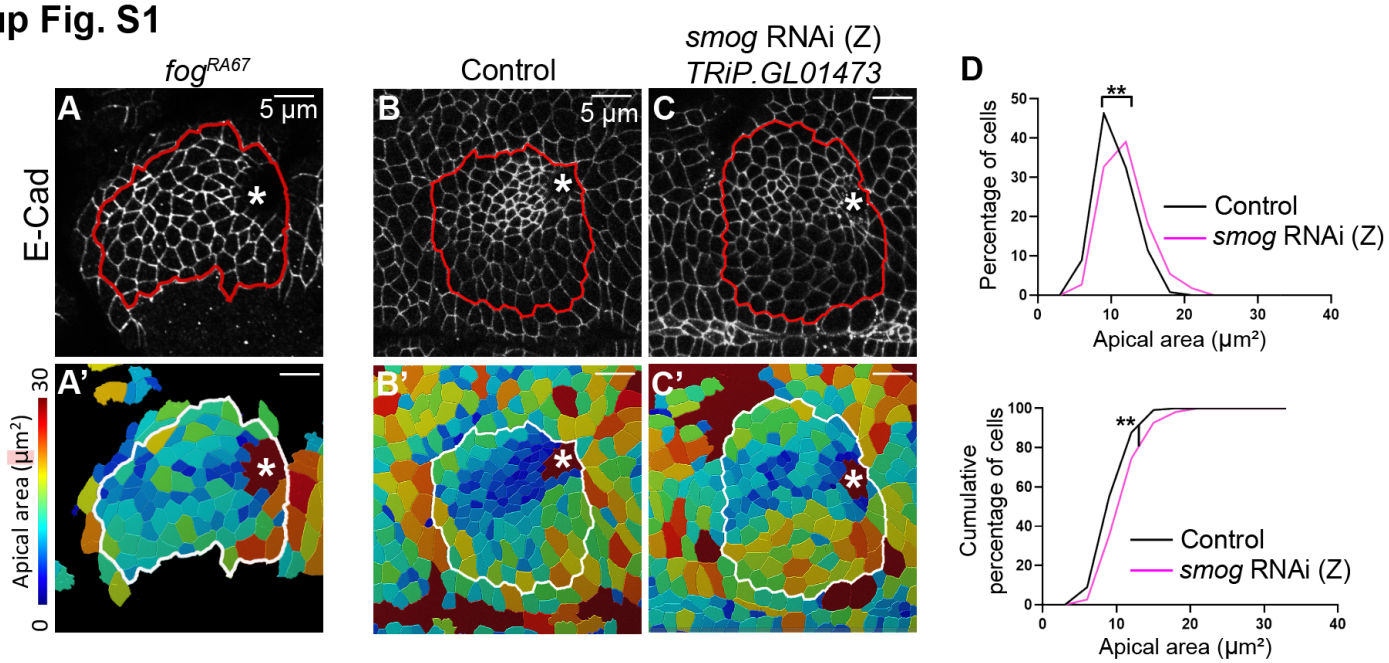
fogRA67
Control
smog RNAi (Z)
TRiP.GL01473
E-Cad
A
B
C
5 µm
5 µm
A'
B'
C'
Apical area (µm²)
30
0
D
Percentage of cells
Apical area (µm²)
Control
smog RNAi (Z)
**
Cumulative percentage of cells
Apical area (µm²)
Control
smog RNAi (Z)
**

Sup. Fig. S2

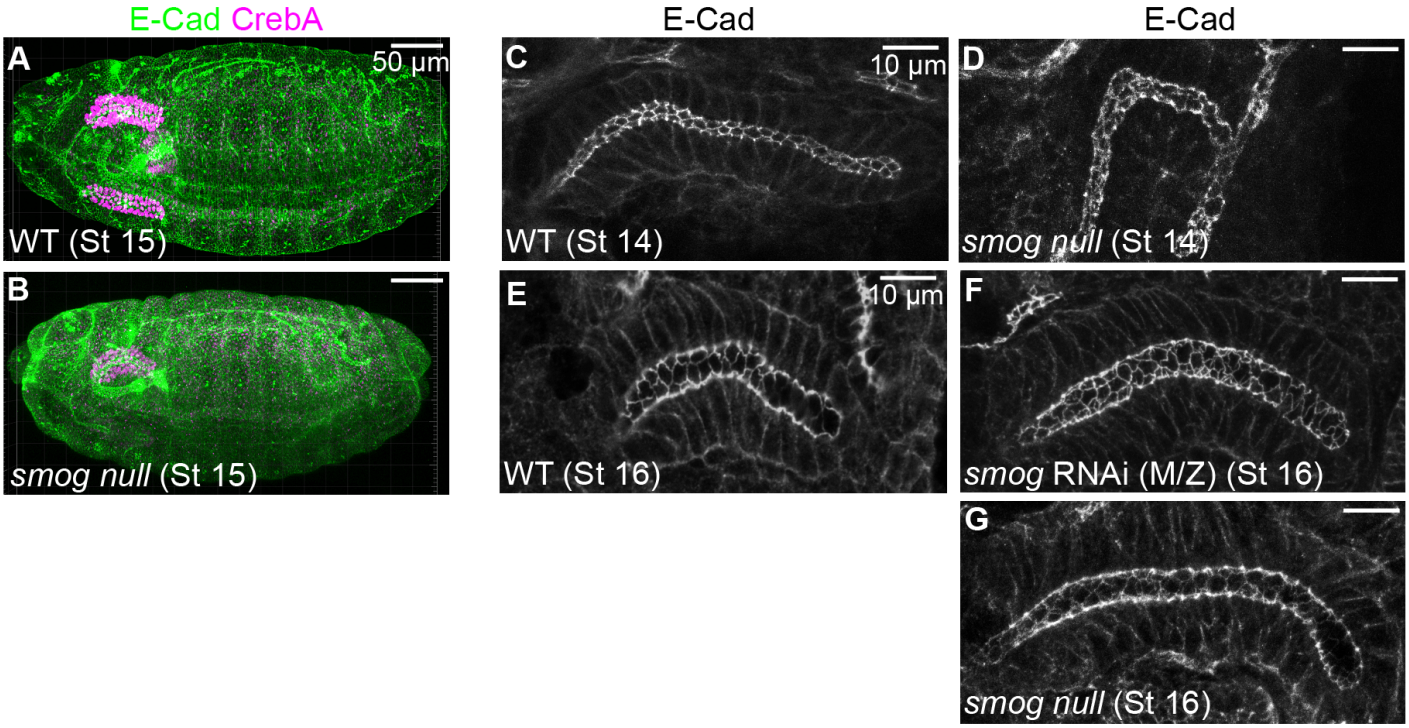
E-Cad CrebA
E-Cad
E-Cad
A
50 µm
WT (St 15)
B
smog null (St 15)
C
10 µm
WT (St 14)
D
smog null (St 14)
E
10 µm
WT (St 16)
F
smog RNAi (M/Z) (St 16)
G
smog null (St 16)

Sup. Fig. S3

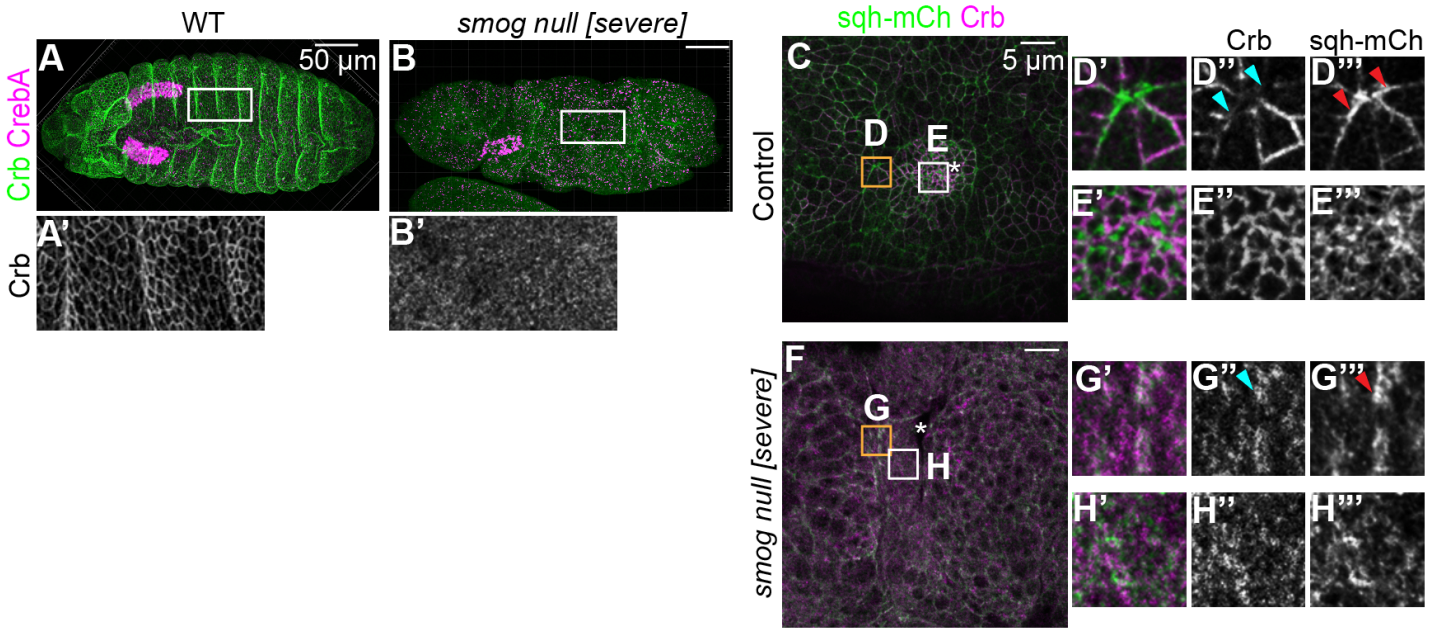
WT
smog null [severe]
Crb CrebA
A
50 µm
B
Crb
A'
B'
sqh-mCh Crb
C
5 µm
Control
D
E
*
Crb
sqh-mCh
D'
D''
D'''
E'
E''
E'''
F
smog null [severe]
G
*
H
G'
G''
G'''
H'
H''
H'''

Sup Fig. S4

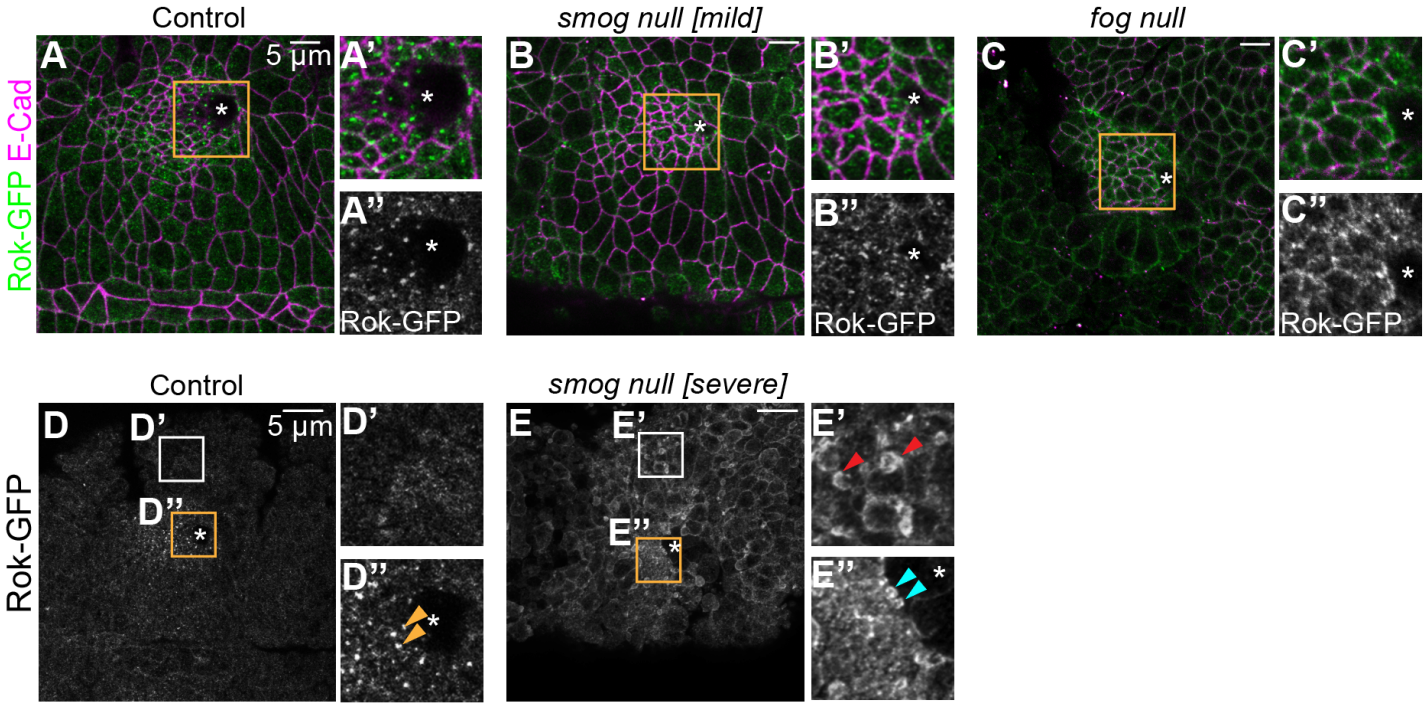
Control
smog null [mild]
fog null
Rok-GFP E-Cad
A
5 µm
A'
A''
B
B'
B''
C
C'
C''
Rok-GFP
Control
smog null [severe]
Rok-GFP
D
D'
D''
5 µm
E
E'
E''